Masses, Radii, and the Equation of State of Neutron Stars

Feryal Özel[1] and Paulo Freire[2]

[1]Department of Astronomy, University of Arizona, Tucson, Arizona 85721; email: fozel@email.arizona.edu

[2]Max-Planck-Institut für Radioastronomie, D-53121 Bonn, Germany; email: pfreire@mpifr-bonn.mpg.de

Annu. Rev. Astron. Astrophys. 2016. 54:401–40

First published online as a Review in Advance on July 27, 2016

The *Annual Review of Astronomy and Astrophysics* is online at astro.annualreviews.org

This article's doi: 10.1146/annurev-astro-081915-023322

Keywords

neutron stars, dense matter, pulsars, pulsar timing, X-ray sources

Abstract

We summarize our current knowledge of neutron-star masses and radii. Recent instrumentation and computational advances have resulted in a rapid increase in the discovery rate and precise timing of radio pulsars in binaries in the past few years, leading to a large number of mass measurements. These discoveries show that the neutron-star mass distribution is much wider than previously thought, with three known pulsars now firmly in the 1.9–2.0-$M_\odot$ mass range. For radii, large, high-quality data sets from X-ray satellites as well as significant progress in theoretical modeling led to considerable progress in the measurements, placing them in the 10–11.5-km range and shrinking their uncertainties, owing to a better understanding of the sources of systematic errors. The combination of the massive-neutron-star discoveries, the tighter radius measurements, and improved laboratory constraints of the properties of dense matter has already made a substantial impact on our understanding of the composition and bulk properties of cold nuclear matter at densities higher than that of the atomic nucleus, a major unsolved problem in modern physics.

Contents

1. INTRODUCTION 402
2. NEUTRON-STAR MASS MEASUREMENTS 404
2.1. Timing Binary Pulsars 404
2.2. Double Neutron-Star Mass Measurements 406
2.3. Millisecond Pulsars 408
2.4. Neutron Stars in X-ray Binaries 412
2.5. Neutron-Star Mass Distribution 413
2.6. Maximum Mass of Neutron Stars 415
3. RADIUS MEASUREMENTS 416
3.1. Spectroscopic Measurements 416
3.2. Radii via Pulse Profile Modeling 421
4. THE NEUTRON-STAR EQUATION OF STATE 424
4.1. Neutron-Star Structure 424
4.2. Constraints on the Equation of State from Low-Energy Experiments 427
4.3. From Radius and Mass Measurements to the Neutron-Star Equation of State 429
4.4. Current Constraints on the Cold Neutron Matter Equation of State 430
5. FUTURE PROSPECTS 432
5.1. The Future of Radio Pulsar Mass Measurements: New Surveys, New Binary Systems, New Measurements, and the Square Kilometre Array 432
5.2. The Future of Radius Measurements 434
5.3. Other Future Probes of Neutron-Star Structure 434

1. INTRODUCTION

Our understanding of neutron stars (NSs) has changed drastically since the first Annual Review article by Wheeler (1966) on this subject, when not a single NS was known and the discussion consisted of an entirely theoretical treatment of collapsed dense stars. The change has been most rapid in the past decade, when the discovery and precisely timed observations of pulsars have proceeded at an ever accelerating rate; the new-generation X-ray and gamma-ray telescopes have provided high-quality, large data sets, and a large body of theoretical work on NS emission properties and spacetimes have enabled significant recent developments in our ability to model these extreme objects and interpret the observations in solid frameworks.

We now know precise masses for ~35 NSs spanning the range from 1.17 to 2.0 $M_\odot$ and can pin down the radii of more than a dozen to the 10–11.5-km range. The combination of the heaviest known NS mass with the existing radius measurements already places significant constraints on the cold dense matter equation of state (EoS) up to densities that are eight times the nuclear density.

Certain characteristics of NSs have been known for a while. Shortly after the discovery of pulsars (Hewish et al. 1968), it became apparent that they are the observational manifestation of extremely compact stars made primarily of neutrons. It was also evident that, though the neutron degeneracy pressure played a role in supporting these compact objects against gravitational collapse, it was not sufficient to hold up a star beyond 0.7 $M_\odot$ (Oppenheimer & Volkoff 1939, Tolman 1939) and that repulsive nuclear forces were necessary in shaping their structure (Harrison et al. 1965). Earlier calculations of the interiors treated nucleons with approximate potentials, predicting masses in the

0.5–3-$M_\odot$ range and radii between 7 and 20 km. Stars of such extreme compactness have central densities that are 5–10 times the nuclear saturation density $\rho_{sat} = 2.8 \times 10^{14}$ g cm^{-3}.

Although the nuclear models improved over the years, the major advances have come from astrophysical observations and models because terrestrial experiments do not approach densities similar to that of NS cores (see Section 4.2). Theoretical work is guided by the well-developed effective field theory approaches and the rapidly developing quantum chromodynamics calculations, but there remain large uncertainties in our understanding of the actual compositions of the cores. Open questions include the composition of matter at high densities, such as the density at which matter needs to be described by quarks and no longer by nucleons, as well as the presence of strangeness or boson condensates in such matter; the isospin symmetry energy that defines the energy difference between normal and neutron-rich matter and, ultimately, the ability to calculate matter in β equilibrium from first principles; and the role and reliability of calculations of N-body interactions. Despite the large number of possibilities, each theoretical model, or its resulting EoS, can be mapped into a mass-radius (M-R) relation by solving the general relativistic structure equations. This, in turn, allows measurements of the NS masses and radii to place strong constraints on the properties and interactions of cold, ultradense matter, as we discuss in this review. These same observations also provide excellent tests of general relativity (GR) in the strong-field regime, using pulsars as well as NS surfaces as test beds.

The recent series of investigations of NS masses and radii are motivated not only by the aim of probing physics in new regimes but also because of the forefront role NSs play in many astrophysical phenomena. NSs are associated with numerous explosive, transient, and nonelectromagnetic events, and NS properties play a role in shaping each one of them. The primary sources of gravitational waves that are expected to be detected with the gravitational wave detector Advanced LIGO (Laser Interferometer Gravitation-Wave Observatory) are the NS–NS and NS–black hole mergers. These systems are also thought to be the central engines of short gamma-ray bursts (see Nakar 2007 for a review). The dynamics of the mergers, the gravitational waveforms in late stages of coalescence, the lifetime of merger disks, and the resulting black hole formation timescales, as well as any accompanying bursts of neutrino, gamma-ray, and/or optical emission, depend sensitively on the NS mass and radius and the EoS (Baiotti et al. 2008, Metzger et al. 2010, Hotokezaka et al. 2011, Bauswein et al. 2012, Lackey et al. 2012, Kumar & Zhang 2015).

From a stellar life cycle and source population point of view, studies of NSs prove to be equally important. Different EoSs allow different maximum masses for NSs and, thus, determine the dividing line between NSs and black holes. This has a direct impact on the outcomes of supernova explosions and the nature of compact remnants, as well as on the numbers of NSs and black holes in the Galaxy. This, in turn, affects the number of observable compact object binaries, their properties, and possible merger/gravitational-wave event rates. In fact, the supernova mechanism itself is affected by the EoS of ultradense matter. The hot dense matter EoS, an extension of the cold one probed by NSs, determines explosion conditions (e.g., Janka et al. 2007) and is crucial for understanding core-collapse supernova explosions and the associated phenomena, including mass loss, r-process nucleosynthesis, and gravitational wave and neutrino emission.

The tremendous advances in the measurements of NS masses, NS radii, and the dense matter EoS have come from a diverse array of techniques, applied to many different populations of NSs, and enabled by observations in all wavelengths from the radio to gamma rays. For example, whereas the precise mass measurements have largely resulted from radio observations of pulsars, the radius measurements have almost exclusively been a result of X-ray observations of NSs in low-mass X-ray binaries (LMXBs). In this review, we focus on the latest mass and radius measurements of NSs and their implications for the dense matter EoS, as well as a number of questions that remain open.

2. NEUTRON-STAR MASS MEASUREMENTS

The vast majority of the precise mass measurements of NSs have been performed using radio observations of rotation-powered pulsars. Currently, more than 2,500 pulsars are known in the Galaxy (Manchester et al. 2005), most of which are detectable as radio pulsars, but also some observed in X-rays and an increasingly large number detected in gamma rays (see **https://confluence.slac.stanford.edu/display/GLAMCOG/Public+List+of+LAT-Detected+Gamma-Ray+Pulsars**) (Abdo et al. 2013, Caraveo 2014).

About 90% of radio pulsars are isolated. Their masses cannot be measured, because all of the current methods rely on precise tracking of the orbital motions through the arrival times of the observed pulsations. The remaining 250 pulsars are located in binary systems (three of these are in multiple component systems). We now focus exclusively on these.

Most of the pulsars in binaries are "recycled": At some point during the evolution of their companions there was mass transfer from the companion to the NS. The mass transfer can, in principle, increase the pulsar mass significantly, but its clearest effect is the spin-up of the pulsar (to spin frequencies as high as 716 Hz; see Hessels et al. 2006) and—by mechanisms that are poorly understood—a sharp reduction in the pulsar's magnetic field, to values smaller than 10^{11} G. This process produces a wide variety of binary pulsars (for a recent review, see, e.g., Lorimer 2008). Those of greatest interest to us are the systems where both components are compact: the double neutron-star (DNS) systems and the millisecond pulsar–white dwarf (MSP-WD) systems.

2.1. Timing Binary Pulsars

The extraordinary long-term rotational stability of recycled pulsars and their fast rotation make them uniquely useful for timing. If a recycled pulsar is in a binary system (as often happens), then we can use this precise timing to measure its orbital motion with astounding precision.

In Newtonian gravity, the part of the orbital motion we can observe (generally along the line of sight only) can be described by five Keplerian parameters: the binary period $P_{\rm b}$, the orbital eccentricity e, the projection of the pulsar's semimajor axis $a_{\rm psr}$ onto the observer's line of sight $x_{\rm psr} = a_{\rm psr} \sin i/c$ (where i is the angle between the orbital angular momentum vector and the line of sight, and c is the speed of light), the time of periastron T_0, and the longitude of periastron ω.

For each new pulsar, these parameters are determined by fitting a radial velocity model to the observed spin periods, which are Doppler shifted by the orbital motion of the pulsar. This is similar to what can be done in spectroscopic systems. The unique feature of pulsars is that, by determining the correct rotational phase count, one can directly range the pulsar relative to the center of mass of the system. Measuring a pulse time of arrival with a precision of 1 μs translates into a ranging accuracy of 300 m per measurement, which is much smaller than the astronomical sizes of the orbits. This provides Keplerian parameters many orders of magnitude more precise than those derived from Doppler shift measurements with the same data and is the reason why pulsars are so useful for such a wide variety of purposes—including uniquely precise mass measurements.

The binary mass function is then determined from the Keplerian orbital parameters

$$f = \frac{(M_{\rm c} \sin i)^3}{M_{\rm T}^2} = \frac{4\pi^2}{T_\odot} \frac{x_{\rm psr}^3}{{P_{\rm b}}^2}, \tag{1}$$

where $\mathrm{T}_\odot \equiv \mathrm{GM}_\odot/c^3 = 4.925490947\ \mu$s is the mass of the Sun in time units (the product $\mathrm{GM}_\odot$, where G is Newton's gravitational constant and $\mathrm{M}_\odot$ is the solar mass, is very precisely known despite the fact that neither G nor $\mathrm{M}_\odot$ is individually known to better than one part in 10^3), and $M_{\rm psr}$, $M_{\rm c}$, and $M_{\rm T} = M_{\rm psr} + M_{\rm c}$ are the pulsar, companion, and total binary masses, respectively,

all expressed in solar masses. This single equation has three unknowns (i, $M_{\rm psr}$, and $M_{\rm c}$); therefore, in the absence of further information, the individual masses $M_{\rm psr}$ and $M_{\rm c}$ cannot be determined despite the high precision in the determination of the Keplerian parameters.

If the projected semimajor axis of the companion's orbit $x_{\rm c}$ can be measured, either via timing, if the companion is a pulsar, or via phase-resolved optical spectroscopy, if the companion is a white dwarf (WD) or main-sequence star, one extra equation is obtained:

$$q \equiv \frac{M_{\rm psr}}{M_{\rm c}} = \frac{x_{\rm c}}{x_{\rm psr}}, \tag{2}$$

which is valid, to first post-Newtonian (PN) order, in all conservative theories of gravity. The number of binary systems in which we can measure q is small, but even for those systems, measuring f and q is not enough to determine the masses. This can be addressed in a few systems because the spectrum of a WD companion allows, in some cases, a determination of its mass, $M_{\rm WD}$ (see Section 2.3.3).

Because of the small sizes of NSs and their NS or WD companions compared with their orbits, both components can be treated as point masses. In this case, the "classical" tidal and rotational effects that complicate the motion of other astrophysical objects and hide the (generally smaller) relativistic effects are simply absent, i.e., such systems are clean gravitational laboratories. In such a system, a pulsar with good timing precision allows the detection and precise measurement of these small relativistic effects. These effects can be parameterized by post-Keplerian (PK) parameters, which, assuming that GR is the correct theory of gravity and to leading PN order, are related to three of the Keplerian parameters ($P_{\rm b}$, x, and e) and the system masses. For the five PK parameters that have been measured in the context of pulsar timing, these expressions are as follows (as in Stairs 2003, and references therein):

1. The rate of advance of periastron $\dot{\omega}$, typically measurable in eccentric orbits. This is analogous to the anomalous perihelion advance in Mercury's orbit:

$$\dot{\omega} = 3\left(\frac{P_{\rm b}}{2\pi}\right)^{-5/3} (\mathrm{T}_\odot M_{\rm T})^{2/3} \left(1-e^2\right)^{-1}. \tag{3}$$

2. The "Einstein delay," γ. In GR, this is due in equal parts to the variations of the gravitational redshift and of special relativistic time dilation in an eccentric orbit:

$$\gamma = e\left(\frac{P_{\rm b}}{2\pi}\right)^{1/3} \mathrm{T}_\odot^{2/3} M_{\rm T}^{-4/3} M_{\rm c}\left(M_{\rm psr}+2M_{\rm c}\right). \tag{4}$$

3. The orbital period decay $\dot{P}_{\rm b}$ due to the loss of orbital energy of the system caused by the emission of gravitational waves (this typically requires timing observations that span many years),

$$\dot{P}_{\rm b} = -\frac{192\pi}{5}\left(\frac{P_{\rm b}}{2\pi \mathrm{T}_\odot}\right)^{-5/3}\left(1+\frac{73}{24}e^2+\frac{37}{96}e^4\right)\times\left(1-e^2\right)^{-7/2} M_{\rm psr} M_{\rm c}\, M_{\rm T}^{-1/3}. \tag{5}$$

4. The range r and the shape s of Shapiro delay, which is a delay in the reception of the radio pulses at the Earth that is due to the propagation of the radio signal in the curved spacetime near the companion star

$$r = \mathrm{T}_\odot M_{\rm c}, \tag{6}$$

$$s = \sin i = x_{\rm psr}\left(\frac{P_{\rm b}}{2\pi}\right)^{-2/3} \mathrm{T}_\odot^{-1/3} M_{\rm T}^{2/3}\, M_{\rm c}^{-1}. \tag{7}$$

This effect is more easily detected in edge-on orbits.

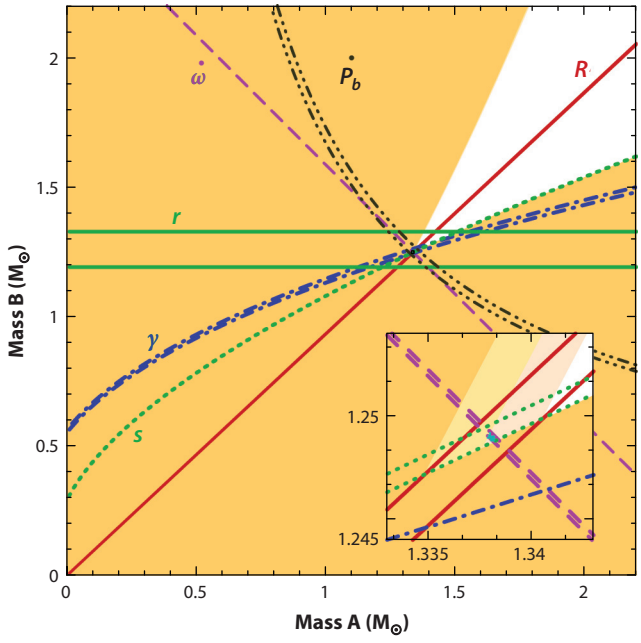

Figure 1

Mass-mass diagram for the J0737−3039 system. The yellow areas are excluded by the mass functions of both pulsars, PSRs J0737−3039A and B. The lines represent the regions allowed by Equations 2–7 for the measured post-Keplerian (PK) parameters. All lines meet at a single point in the diagram, i.e., general relativity passes the tests posed by these four distinct constraints. This plot is important because it indicates that we get consistent mass measurements using any pair of PK parameters. Adapted from Kramer et al. (2006) with permission.

We must here emphasize that, like the Keplerian parameters, these are parameters that appear in the equations that describe the motion and timing of binary pulsars, such as those presented by Damour & Deruelle (1985, 1986). They are measured by timing a particular system and fitting the pulse arrival times. It is only when we adopt a specific theory of gravity that we can relate them to physical parameters of the components of the binary—in the case of GR, and to leading PN order, we can relate them to their masses only (Equations 3–7). These constraints are displayed graphically in **Figure 1**. Note that there is nothing unique about the particular parameterization of Damour & Deruelle (1985). As an example, instead of r and s, we can describe Shapiro delay with two less-correlated PK parameters, ς and h_3 (Freire & Wex 2010).

2.2. Double Neutron-Star Mass Measurements

The first system for which reliable mass measurements were made was PSR B1913+16, the first binary pulsar ever discovered (Hulse & Taylor 1975). The compact orbit of this DNS (P_b = 0.32299 days) and its high orbital eccentricity [$e = 0.6171334(5)$] allowed a precise measurement of the PK parameter $\dot{\omega}$. Subsequently, Taylor et al. (1979) were able to measure two more PK parameters, γ and $\dot{P}_\mathrm{b}$. The individual masses were determined from Equations 3 and 4, and the observed orbital decay was then used as a successful test of GR. The GR prediction for $\dot{P}_\mathrm{b}$ caused by gravitational wave emission (Equation 5) for the derived masses was consistent with the observed rate (see Damour 2015 for a review).

Table 1 Masses of double neutron-star systems and nonrecycled pulsars[a]

System	M_T ($M_\odot$)	M_{psr} ($M_\odot$)	M_c ($M_\odot$)	Mass constraint	References
Systems with well-measured component masses					
J0453+1559	2.734 (4)	1.559 (5)	1.174 (4)	$\dot{\omega}, h_3$	Deneva et al. (2013), Martinez et al. (2015)
J0737−3039	2.58708 (16)	1.3381 (7)	1.2489 (7) y	$\dot{\omega}, q$	Kramer et al. (2006)
B1534+12	2.678463 (8)	1.3330 (4)	1.3455 (4)	$\dot{\omega}, \gamma$	Fonseca et al. (2014)
J1756−2251	2.56999 (6)	1.341 (7)	1.230 (7)	$\dot{\omega}, \gamma$	Ferdman et al. (2014)
J1906+0746	2.6134 (3)	1.291 (11) y	1.322 (11) ?	$\dot{\omega}, \gamma$	van Leeuwen et al. (2015)
B1913+16	2.828378 (7)	1.4398 (2)	1.3886 (2)	$\dot{\omega}, \gamma$	Weisberg et al. (2010)
B2127+11C g	2.71279 (13)	1.358 (10)	1.354 (10)	$\dot{\omega}, \gamma$	Jacoby et al. (2006)
Systems with total binary mass measurement only					
J1518+4904	2.7183 (7)	<1.768	>0.950	$\dot{\omega}$	Janssen et al. (2008)
J1811−1736	2.57 (10)	<1.64	>0.93	$\dot{\omega}$	Corongiu et al. (2007)
J1829+2456	2.59 (2)	<1.34	>1.26	$\dot{\omega}$	Champion et al. (2005)
J1930−1852	2.59 (4)	<1.32	>1.30	$\dot{\omega}$	Swiggum et al. (2015)
Nonrecycled pulsars with massive white dwarf companions					
J1141−6545	2.2892 (3)	1.27 (1) y	1.01 (1)	$\dot{\omega}, \gamma$	Bhat et al. (2008), Antoniadis et al. (2011)
B2303+46	2.64 (5)	1.24–1.44 y	1.4–1.2	$\dot{\omega}, M_{WD}$	Thorsett & Chakrabarty (1999), van Kerkwijk & Kulkarni (1999)

[a]The systems indicated with a "g" are located in globular clusters. A question mark "?" indicates that the neutron-star (NS) nature of the companion is not firmly established. The mass measurements for NSs detected as normal (nonrecycled) radio pulsars are indicated with the letter "y." References are to the latest mass measurements.

A number of other DNSs have since been discovered. The eleven systems for which mass constraints are known are listed in the top two groups in **Table 1**, together with the latest references. These systems are relatively rare, making up about 5% of the currently known population of binary pulsars. We list the total mass M_T of each binary because, generally, that is much better known than the individual masses of the components. This happens because the orbits of all DNSs are eccentric, so that $\dot{\omega}$ (and M_T) can be determined with high precision. In binaries where additional PK parameters are measured, we also list the individual NS masses and specify the parameters that were measured to derive the masses (for all these systems, Equation 1 can be used to determine the orbital inclination i). For one of these systems (J1906+0746) it is possible for the companion to be a massive WD instead. PSR B2127+11C is located in the globular cluster (GC) M15 and is very likely the result of an exchange interaction (Prince et al. 1991).

PSR B1913+16 is no longer unique in providing a stringent test of GR. The orbital decay due to the emission of gravitational waves has been measured for five other DNS systems (J0737−3039A/B, B1534+12, J1756−2251, J1906+0746, and B2127+11C), and, as we discuss below, a few MSP-WD systems as well.

We also include in **Table 1** two radio pulsars that have precise mass measurements even though they are not members of DNS systems. Their slow spins and higher magnetic fields indicate that they have not been recycled, making them resemble DNSs rather than the MSP-WD companions that we discuss in Section 2.3.

2.2.1. The double pulsar. Among the DNS population, one system in particular stands out: J0737−3039. This system is a unique laboratory for gravitational physics because it combines an unusual number of desirable features: (*a*) With an orbital period of 2 h 27 m, it is by far the most compact DNS known. Combined with the moderate orbital eccentricity of the system, this implies that the PK parameters $\dot{\omega}$, γ, and $\dot{P}_b$ are relatively large and easy to measure, promising one precise test of GR. (*b*) The system has a high orbital inclination, $i \sim 89°$. This allows for a precise measurement of the two Shapiro delay parameters, r and s, thus providing two more independent tests of GR. (*c*) The second NS in the system is also an active radio pulsar, which is detectable at least some of the time (Lyne et al. 2004). This makes it the only currently known double pulsar system and allows a precise measurement of the mass ratio, q, which "frees" one of the PK parameters from the role of mass determination and, therefore, allows one more test of GR.

The four tests in this system provided by Equations 3–7 are remarkably stringent, but despite that, GR has passed all of them (Kramer et al. 2006). This can be seen in **Figure 1**, where all the regions compatible with the known mass constraints are consistent with the same pair of masses. Such tests of gravity theories are not the topic of this review—we refer interested readers to Wex (2014) for a comprehensive discussion. Nevertheless, systems like J0737−3039 and **Figure 1** are important for NS mass measurements because they demonstrate experimentally that any pair of mass constraints chosen from q and the PK parameters will generally yield consistent NS masses.

2.3. Millisecond Pulsars

The term millisecond pulsars (MSPs) refers to pulsars with spin periods in the range of $1.39 < P < 20$ ms and $\dot{P} < 10^{-19}$. These systems have been heavily recycled (and circularized) by a long-lived accretion phase in an LMXB. The first MSP by this definition, B1937+21, was discovered using the Arecibo telescope in 1982 (Backer et al. 1982). (At a 642-Hz spin frequency, this was the fastest known MSP for the subsequent 24 years.) A great number of MSPs have been discovered since and, although ∼20% are isolated, most of the remaining objects have WD companions and very small orbital eccentricities.

The fast (and very stable) rotation of MSPs makes their timing significantly more precise than that for the pulsars in DNSs. However, their low orbital eccentricities pose a problem for mass determination (and tests of GR), because, in these cases, the PK parameters $\dot{\omega}$ and especially γ cannot be measured accurately. Furthermore, most systems have orbital periods larger than 0.5 days, which makes a detection of the very small predicted values of $\dot{P}_b$ nearly impossible. These difficulties made the measurement of MSP masses a slow and difficult process. Four strategies have been followed over the past two decades, which have recently started producing a number of precise mass measurements.

2.3.1. Pulsars in globular clusters. One way of getting around the issue of orbital circularity is to find MSPs in GCs. Because of the much higher stellar density, there are substantial gravitational interactions with nearby stars that, with time, can make an initially circular orbit acquire a substantial eccentricity. This allows the measurement of $\dot{\omega}$ and, if there are no classical contributions to this effect, the total mass of the system M_T for quite a few systems (see **Table 2**).

The first binary mass precise enough to be useful was that of PSR J0024−7204H, a 3.21-ms pulsar in a 2.35-day, slightly eccentric [$e = 0.070560(3)$] orbit around a low-mass WD in the GC 47 Tucanae, which yielded $M_T = 1.61 \pm 0.04\,M_\odot$ (Freire et al. 2003). No further PK parameters were measurable; nevertheless, one can infer from combining Equations 1 and 3 (and

Table 2 Masses of millisecond pulsars[a]

System	M_T ($M_\odot$)	M_{psr} ($M_\odot$)	M_c ($M_\odot$)	Mass constraint	References
Millisecond pulsars with white dwarf companions and low-eccentricity orbits					
J0348+0432		2.01 (4)	0.172 (3)	q, M_{WD}	Antoniadis et al. (2013)
J0437−4715		1.44 (7)	0.224 (7)	r, s	Reardon et al. (2016)
J0621+1002	2.32 (8)	$1.53^{+0.10}_{-0.20}$	$0.76^{+0.28}_{-0.07}$	$\dot{\omega}$, s	Kasian (2012)
J0751+1807		1.64 (15)	0.16 (1)	s, $\dot{P}_b$	Desvignes et al. (2016)
J1012+5307		1.83 (11)	0.16 (2)	q, M_{WD}	Antoniadis (2016)
J1614−2230		1.928 (7)	0.500 (6)	r, s	Fonseca et al. (2016)
J1713+0747		1.31 (11)	0.286 (12)	r, s	Zhu et al. (2015)
J1738+0333		$1.47^{+0.07}_{-0.06}$	$0.181^{+0.007}_{-0.005}$	q, M_{WD}	Antoniadis et al. (2012)
J1802−2124		1.24 (11)	0.78 (4)	r, s	Ferdman et al. (2010)
J1807−2500B	2.57190 (73)	1.3655 (21)	1.2064 (20) ?	$\dot{\omega}$, h_3	Lynch et al. (2012)
B1855+09		$1.31^{+0.12}_{-0.10}$	$0.238^{+0.013}_{-0.012}$	r, s	Fonseca et al. (2016)
		$1.59^{+0.21}_{-0.18}$	$0.268^{+0.022}_{-0.019}$	r, s	Desvignes et al. (2016)
J1909−3744		1.55 (3)	0.214 (3)	r, s	Fonseca et al. (2016), Desvignes et al. (2016)
J1918−0642		$1.19^{+0.10}_{-0.09}$	$0.219^{+0.012}_{-0.011}$	r, s	Fonseca et al. (2016)
J2222−0137		1.20 (14)	1.05 (6)	r, s	Kaplan et al. (2014a)
Millisecond pulsars with eccentric orbits and triples					
J0337+1715		1.4378 (13)	0.19751 (15)	i, q	Ransom et al. (2014)
			0.4101 (3)		Kaplan et al. (2014b)
J1903+0327	2.697 (29)	1.667 (21)	1.029 (8)	$\dot{\omega}$, h_3	Freire et al. (2011)
J1946+3417	2.097 (13)	1.832 (13)[b]	0.2659 (11)	$\dot{\omega}$, h_3	E.D. Barr, P.C.C. Freire, M. Kramer, and D. Champion (in preparation)
J2234+0611	1.668 (6)	1.393 (13)[b]	0.276 (9)	$\dot{\omega}$, h_3	K. Stovall, P. Freire, J. Deneva, M. McLaughlin, and J. Martinez (in preparation)
Millisecond pulsars in globular clusters					
J0024−7204H	1.61 (4)	<1.52	>0.164	$\dot{\omega}$	Freire et al. (2003)
J0514−4002A	2.453 (14)	<1.50	>0.96	$\dot{\omega}$	Freire et al. (2007)
B1516+02B	2.29 (17)	<2.52	>0.13	$\dot{\omega}$	Freire et al. (2008a)
J1748−2021B	2.92 (20)	<3.24	>0.11	$\dot{\omega}$	Freire et al. (2008b)
J1748−2446I	2.17 (2)	<1.96	>0.24	$\dot{\omega}$	Ransom et al. (2005)
J1748−2446J	2.20 (4)	<1.96	>0.38	$\dot{\omega}$	Ransom et al. (2005)
J1750−37A	1.97 (15)	<1.65	>0.53	$\dot{\omega}$	Freire et al. (2008b)
B1802−07	1.62 (7)	<1.7	>0.23	$\dot{\omega}$	Thorsett & Chakrabarty (1999)
J1824−2452C	1.616 (7)	<1.35	>0.26	$\dot{\omega}$	Bégin (2006)
J1910-5958A		1.3 (2)	0.180 (18)	q, M_{WD}	Bassa et al. (2006), Cocozza et al. (2006)

[a]J1807−2500B is located in the globular cluster NGC 6544. A question mark "?" indicates that the nature of the companion is uncertain. The total mass is indicated only when it is known more precisely than the masses of the components. References are to the latest mass measurements.
[b]Preliminary values.

the mathematical fact $\sin i \leq 1$) that $M_{\rm psr} < 1.52\ M_\odot$. This was one of the earlier indications that the long recycling episodes that spin up MSPs do not necessarily make them very massive.

Since the discovery of that system, most eccentric systems found in GCs have shared the same characteristic: We can measure $\dot{\omega}$ but no other mass constraints. The reason for this is that the most eccentric systems tend to be the ones with wider orbits, which are more easily perturbed by nearby stars. For these relatively wide orbits, it is very difficult to measure γ and $\dot{P}_{\rm b}$.

The two exceptions are two of the exchange encounter systems listed in **Tables 1** and **2**, B2127+11C and J1807–2500B. Both are located in clusters with collapsed cores, where exchange encounters are more likely (Verbunt & Freire 2014). The orbital period of B2127+11C is 8.0 h and its orbital eccentricity is 0.681386(16), which allows measurements of $\dot{\omega}$, γ, and even $\dot{P}_{\rm b}$ (Jacoby et al. 2006). The last system, J1807−2500B, is particularly important for this discussion: It is a true MSP with a spin period of 4.18 ms, but despite the long accretion episode, its current mass is only 1.3655 (21) $M_\odot$. More than any other system, this MSP demonstrates that full recycling can be achieved without a large mass increment.

Nevertheless, as the number of $M_{\rm T}$ measurements accumulated, it became apparent that some systems, such as PSRs J1748−2446I and J in Terzan 5 (Ransom et al. 2005), PSR J1748−2021B in NGC 6440 (Freire et al. 2008b), and PSR B1516+02B in M5 (Freire et al. 2008a), are quite massive but have very low-mass functions. This is only likely to happen if the pulsars and not the companions in these systems are massive. Indeed, by 2008, there was already strong evidence that a fair fraction of MSPs must have masses close to 2 $M_\odot$ (Freire et al. 2008a). This statistical result was confirmed by the later MSP mass measurements, described below.

2.3.2. Shapiro delay measurements. For the vast majority of pulsar-WD systems, the only measurable PK parameters are those related to the Shapiro delay. However, the fastest-spinning MSPs tend to have very low-mass helium WD companions, which reduces the amplitude of the Shapiro delay. Therefore, in order to measure the masses in these systems, both a very good timing precision and a high orbital inclination are required.

The first MSP-WD system where the Shapiro delay was clearly detected was PSR B1855+09 (Ryba & Taylor 1991). However, until recently, the timing precision in this system was not enough for a precise determination of the pulsar mass. This changed in 2003 with the discovery of PSR J1909−3744, a heavily recycled MSP with $P = 2.9$ ms and a light helium WD companion (Jacoby et al. 2003). This system combines high timing accuracy with a high orbital inclination, which allowed, in 2005, the first precise measurement of the mass of an MSP (Jacoby et al. 2005).

Since then, the number of MSPs discovered has been increasing significantly (see Section 5.1), and for that reason the number of precise Shapiro delay mass measurements has been accumulating, particularly for pulsars with more massive carbon-oxygen or oxygen-neon-magnesium WD companions, such as PSR J1802−2124 (Ferdman et al. 2010) or more recently PSR J2222−0137 (Kaplan et al. 2014a). The larger companion masses make the Shapiro delay easier to measure; this is why a disproportionate number of MSPs with well-measured masses have such massive companions. This does not apply as a rule to the MSPs themselves: The latter systems highlight the fact that many NSs are born with masses as low as ∼1.2 $M_\odot$.

Of these MSPs with massive WD companions, the measurement that had by far the greatest impact was PSR J1614−2230 (Demorest et al. 2010). The originally reported mass of the pulsar was 1.97 (4) $M_\odot$, which was exceptional and unexpected among the MSPs with massive WD companions. This mass measurement had implications for the NS mass distribution as well as for the NS EoS, which are discussed in later sections (see Sections 2.5 and 4, respectively). Note that this measurement has since been slightly improved, which revised the mass to $M = 1.928\ (17)\ M_\odot$ (Fonseca et al. 2016), a value that is still consistent with the earlier value.

2.3.3. Spectroscopic mass measurements. For some of the MSPs, particularly those with short orbital periods, the companion is optically bright. This has allowed reliable mass determinations of both components by studying the Balmer lines produced by hydrogen in the WD atmosphere.

First, phase-resolved spectroscopy can measure how these lines shift with orbital phase, providing a measurement of the projected orbital velocity of the WD. Comparing this with the orbital velocity of the pulsar measured in the timing ($v_{\rm psr} = 2\pi x_{\rm psr}/P_{\rm b}$), we can immediately determine the mass ratio, $q \equiv M_{\rm psr}/M_{\rm WD} = v_{\rm WD}/v_{\rm psr}$.

Second, the width of the Balmer lines is related to the local gravitational acceleration, $g = GM_{\rm WD}/R_{\rm WD}^2$. Using model relations between $M_{\rm WD}$ and $R_{\rm WD}$ for WDs (see, e.g., the references in Antoniadis et al. 2012), both quantities can be determined from g. After this step $M_{\rm psr}$ can be obtained trivially from $qM_{\rm WD}$.

The first such measurement was made for PSR J1012+5307 (Callanan et al. 1998), later followed by the mass measurement for J1910−5958A, an MSP-WD system in NGC 6752 (Bassa et al. 2006, Cocozza et al. 2006). To date, the two most important such measurements have been those of J1738+0333 (Antoniadis et al. 2012) and J0348+0432 (Antoniadis et al. 2013, Lynch et al. 2013). For the former $M_{\rm psr} = 1.47^{+0.07}_{-0.06}$ $M_\odot$ and $M_{\rm WD} = 0.181^{+0.007}_{-0.005}$ $M_\odot$; this measurement was important because the relatively short orbital period (8.5 h) allowed a measurement of $\dot{P}_{\rm b}$ (Freire et al. 2012), which agrees with the GR prediction for these masses. Given the asymmetry in the binding energy of this system, this measurement introduced the most stringent constraints ever for several families of gravity theories (Freire et al. 2012), superseding the previous test from the pulsar-WD system PSR J1141−6545 (Bhat et al. 2008).

For PSR J0348+0432, a pulsar with a WD companion having an orbital period of only 2h 27m, Antoniadis et al. (2013) obtained $M_{\rm psr} = 2.01\ (4)\ M_\odot$ and $M_{\rm WD} = 0.172\ (3)\ M_\odot$. This confirmed, using a different method, that NSs could reach masses of the order of 2 $M_\odot$. Furthermore, the short orbital period has allowed a measurement of $\dot{P}_{\rm b}$ (Antoniadis et al. 2013), which again agrees with the GR prediction and has already placed significant constraints on nonlinear phenomena predicted by some alternative theories of gravity for these massive NSs, such as spontaneous scalarization (Damour & Esposito-Farèse 1996).

2.3.4. Triples, disrupted triples, and other monsters. The theoretical expectation that the recycling pathway for fast MSPs result in highly circular orbits was corroborated by the fact that all fully recycled MSPs outside of GCs observed until 2008 had orbital eccentricities between 10^{-7} and 10^{-3} (Manchester et al. 2005). In 2008, the situation changed with the discovery of PSR J1903+0327 (Champion et al. 2008). This fast-spinning MSP ($P = 2.15$ ms) is in a binary system with an ∼1-$M_\odot$ main-sequence-star companion in a 95-day, eccentric orbit ($e = 0.44$). This system is thought to have originated from a hierarchical triple that became chaotically unstable, as suggested by observational data (Freire et al. 2011) and numerical simulations (Portegies Zwart et al. 2011). This finding suggested triple stellar systems containing MSPs might still be found in the Galaxy, which was later confirmed with the discovery of PSR J0337+1715, the first MSP in a stellar triple system with two WD companions (Ransom et al. 2014). Note that the mass indicated in **Table 2** for PSR J0337+1715 is based on these triple interactions.

Soon after the discovery of PSR J1903+0327, Bailes (2010) reported an "anomalous" orbital eccentricity of 0.027 for PSR J1618−3919, a 12-ms pulsar first reported by Edwards & Bailes (2001) that is in a 22-day orbit with a low-mass WD companion. More recently, Deneva et al. (2013), Barr et al. (2013), Knispel et al. (2015), and Camilo et al. (2015) reported the discovery of four more unusual binary MSP systems with eccentric orbits: PSRs J2234+06, J1946+3417, J1950+2414, and J0955−6150. These four systems are fully recycled with spin periods between 2 and 4.4 ms, orbital periods from 22 to 32 days, and median companion masses $M_{\rm c} \approx 0.25$ $M_\odot$;

i.e., apart from their large orbital eccentricities ($0.07 < e < 0.14$) all parameters are compatible with the canonical recycling formation channel leading to an MSP with a WD companion. (For a discussion on their unusual formation, see Knispel et al. 2015.)

The reason why these systems are mentioned at length here is that for nearly all of them, precise mass measurements have been, or will soon be, made. For PSRs J1903+0327, J1946+3417, and J2234+0611, precise mass measurements have been obtained from the combination of $\dot{\omega}$ and the Shapiro delay parameter h_3 [Freire et al. 2011; also K. Stovall, P. Freire, J. Deneva, M. McLaughlin, and J. Martinez (in preparation) and E.D. Barr, P.C.C. Freire, M. Kramer, and D. Champion, (in preparation)]. Note that for PSR J1903+0327, the uncertainty quoted in **Table 2** corresponds to 99.7% confidence level (C.L.). A similar measurement will certainly be possible for PSR J1950+2414. For the triple system, even more precise masses for the MSP and two WD companions could be obtained from the 3-body effects in the system (Ransom et al. 2014).

The masses in these systems are quite varied. Although the MSPs in the triple system J0337+1715 and in the eccentric binary system J2234+0611 (K. Stovall, P. Freire, J. Deneva, M. McLaughlin, and J. Martinez, in preparation) have masses of 1.4378 (13) $M_\odot$ and 1.393 (13) $M_\odot$, respectively, PSR J1946+3417 is in the massive NS group, with $M_{\rm psr} = 1.832$ (13) $M_\odot$ (E.D. Barr, P.C.C. Freire, M. Kramer, and D. Champion, in preparation). PSR J1903+0327 sits in the middle, with $M_{\rm psr} = 1.667$ (21) $M_\odot$ (99.7% C.L.). (The error bars for this measurement are not Gaussian, and therefore the 68% error bar is not 1/3 of this uncertainty; see Freire et al. 2011 for a discussion.)

2.4. Neutron Stars in X-ray Binaries

Mass measurements have also been carried out for NSs with high and low stellar mass companions using the observations of these binaries in X-ray and optical wavelengths. We discuss the methods and results for these two classes below.

2.4.1. Neutron stars with high-mass companions. For mass measurements of NSs with high-mass companions, eclipsing X-ray pulsars, in which the companions block the X-rays from the pulsar for part of the orbit, form the primary targets. In these systems, X-ray observations of the pulsar yield the orbital period of the binary $P_{\rm b}$, the eccentricity of the orbit e, the longitude of periastron ω_0, the semimajor axis of the NS's orbit $a_X \sin i$, and the semiduration of the eclipse θ_e. In addition, optical observations of the companion star give its velocity amplitude $K_{\rm opt}$, its projected rotational velocity $v_{\rm rot} \sin i$, and the amplitude of ellipsoidal variations A. From these observables, it is possible to solve for the fundamental parameters of the binary, which include the mass of the NS $M_{\rm NS}$; the mass, radius, and rotational angular velocity of the companion $M_{\rm opt}$, $R_{\rm opt}$, and $\Omega_{\rm opt}$; and the inclination angle of the binary i.

These measurements are typically less precise than those obtained from radio pulsar timing, and several sources of systematic uncertainty in this technique are discussed by Özel et al. (2012b) and Falanga et al. (2015). The ten NSs whose masses have been estimated in this way are listed in **Table 3**.

2.4.2. Neutron stars in low-mass X-ray binaries. Spectral studies of thermonuclear X-ray bursts from NSs provide simultaneous measurements of their masses and radii. These mass constraints are less precise than those obtained from pulsar timing but still provide an estimate of NS masses in a different population. The details of the methods are discussed in Section 3.1, and the mass measurements for the six sources in this category are listed in **Table 3**. This table also

Table 3 Masses of neutron stars in high-mass and low-mass X-ray binaries[a]

System	M_{NS} ($M_\odot$)	Error ($M_\odot$)	References
Neutron stars in high-mass X-ray binaries			
LMC X−4	1.57	0.11	1
Cen X−3	1.57	0.16	1
4U 1538−522	1.02	0.17	1
SMC X−1	1.21	0.12	1
SAX J1802.7−2017	1.57	0.25	1
XTE J1855−026	1.41	0.24	1
Vela X−1	2.12	0.16	1
EXO 1722−363	1.91	0.45	1
OAO 1657−415	1.74	0.30	1
Her X−1	1.07	0.36	1
Neutron stars in low-mass X-ray binaries			
4U 1608−52	1.57	$^{+0.30}_{-0.29}$	2
4U 1724−207	1.81	$^{+0.25}_{-0.37}$	2
KS 1731−260	1.61	$^{+0.35}_{-0.37}$	2
EXO 1745−248	1.65	$^{+0.21}_{-0.31}$	2
SAX J1748.9−2021	1.81	$^{+0.25}_{-0.37}$	2
4U 1820−30	1.77	$^{+0.25}_{-0.28}$	2
Cyg X−2	1.90	$^{+0.22}_{-0.35}$	3

[a]We exclude 4U 1700−377, for which there is no evidence that it is a neutron star. References are to the latest constraints. References: 1. See Rawls et al. (2011), Özel et al. (2012b), Falanga et al. (2015), and references therein. 2. See Özel et al. (2016). 3. See Orosz & Kuulkers (1999).

includes the LMXB Cyg X−2, for which the mass of the NS was inferred using optical observations of its companion.

2.5. Neutron-Star Mass Distribution

We show in **Figure 2** the combined NS mass measurements in all of the above categories. It is already clear from this figure that current measurements show a broad range of NS masses, from ≈1.1–2 $M_\odot$. The differences between the NS masses in different categories are also evident. To study and characterize the mass distributions of these different classes in more detail, it is possible to use Bayesian statistical techniques on the currently available measurements. In particular, the three different categories of sources, namely, the DNSs, the slow pulsars (i.e., the small spin period pulsars and NSs with high-mass companions, which are likely to be near their birth masses), and the recycled pulsars (which include all MSPs and the accreting NSs with low-mass companions), can each be modeled with Gaussian functions with a mean of M_0 and a dispersion σ:

$$P(M_{NS}; M_0, \sigma) = \frac{1}{\sqrt{2\pi\sigma^2}} \exp\left[-\frac{(M_{NS} - M_0)^2}{2\sigma^2}\right]. \quad (8)$$

Several studies have employed Bayesian techniques to measure the most likely values of the mean and dispersion for these systems (Özel et al. 2012b, Kiziltan et al. 2013). **Figure 3** shows the inferred mass distributions for these different categories of NSs. The most likely values of the

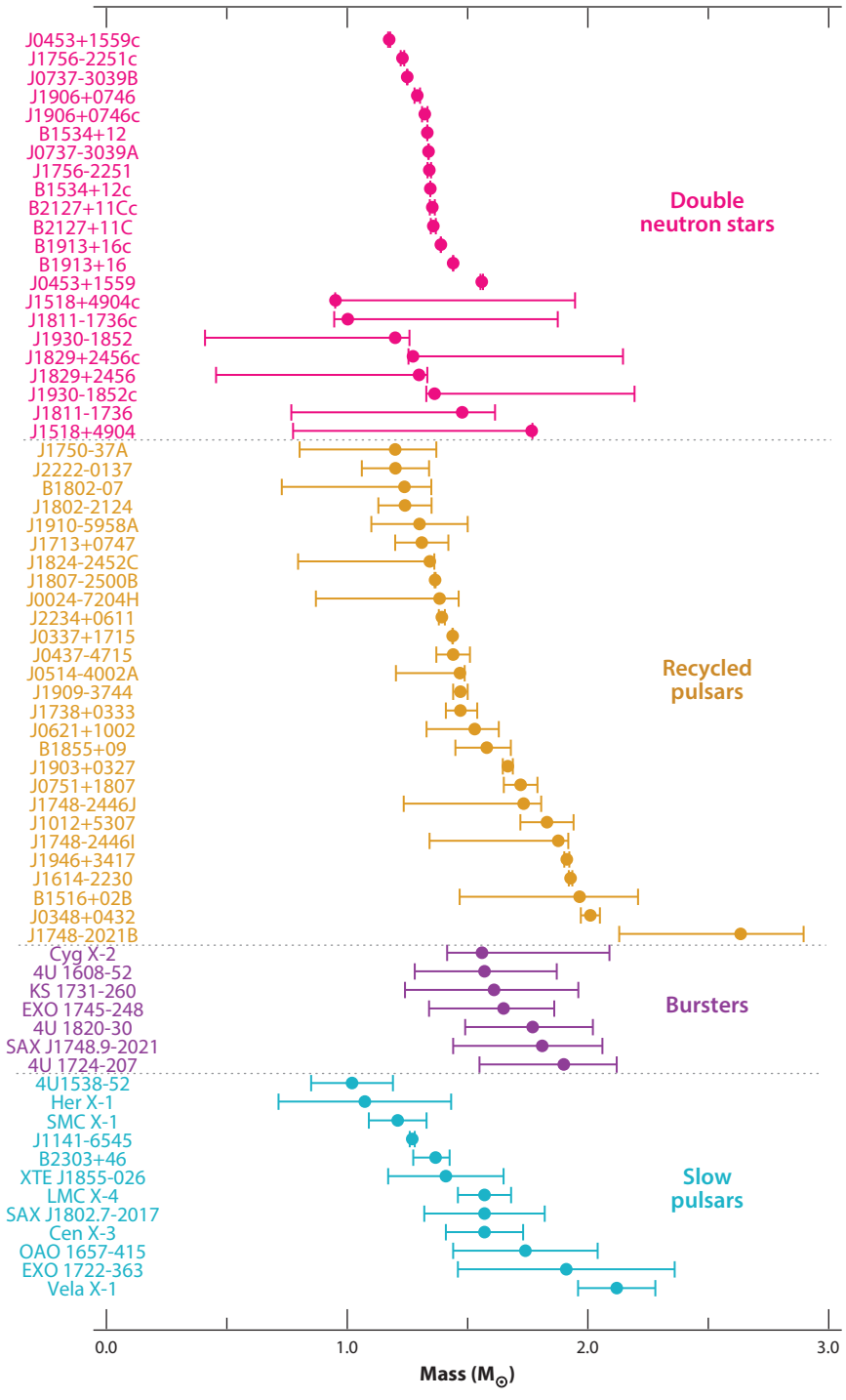

Figure 2

The most recent measurements of neutron-star masses. Double neutron stars (*magenta*), recycled pulsars (*gold*), bursters (*purple*), and slow pulsars (*cyan*) are included.

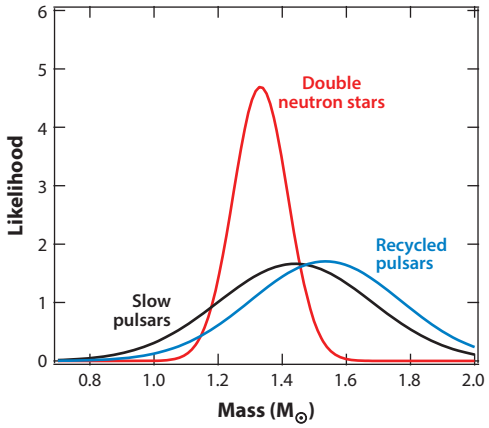

Figure 3

The inferred mass distributions for the different populations of neutron stars.

parameters for these distributions are the following: $M_0 = 1.33\ M_\odot$ and $\sigma = 0.09\ M_\odot$ for the DNSs, $M_0 = 1.54\ M_\odot$ and $\sigma = 0.23\ M_\odot$ for the recycled NSs, and $M_0 = 1.49\ M_\odot$ and $\sigma = 0.19\ M_\odot$ for the slow pulsars. A recent study also raised the possibility of two peaks within the recycled MSP population, with the first peak at $M = 1.39\ M_\odot$ and a dispersion $\sigma = 0.06\ M_\odot$ and a second peak appearing at $M = 1.81\ M_\odot$ with a dispersion of $\sigma = 0.18\ M_\odot$ (Antoniadis et al. 2016).

Among these inferred distributions, the narrowness of the DNS distribution stands out. Although clearly not representative of NSs as a whole, as it was once thought (Thorsett & Chakrabarty 1999), it probably points to a particular evolutionary mechanism that keeps the masses of NSs in these systems in a narrow range. Recent discoveries, such as the DNS J0453+1559 (Deneva et al. 2013), indicate that the range of masses in DNS systems may also be wider than previously believed: the recycled pulsar has a mass of 1.559 (5) $M_\odot$, the heaviest known in any DNS (Martinez et al. 2015), whereas the companion has a mass of 1.174 (4) $M_\odot$, the smallest precisely measured mass of any NS (we infer that the companion is an NS from the orbital eccentricity of the system, $e = 0.11251837(5)$, which would not arise if it had slowly evolved to a massive WD star).

2.6. Maximum Mass of Neutron Stars

Finding the maximum mass of NSs is of particular interest in mass measurements because of its direct implications for the NS EoSs and NS evolution. The largest NS mass can rule out the EoSs that have maximum masses and fall below this value. The current record holder on this front is J0348+0432 with a mass of $2.01 \pm 0.04\ M_\odot$ (Antoniadis et al. 2013).

There are also some studies of a particular class of MSPs called black widows (and their cousins redbacks) that have suggested higher NS masses (e.g., van Kerkwijk et al. 2011). These MSPs irradiate and ablate their very low-mass companions. Although the pulsar timing provides the Keplerian parameters for the orbit, all other information about the masses in these systems is obtained from the modeling of the optical light curves (to determine orbital inclination) and the spectroscopy (to measure the mass ratio) of the companion star. Unfortunately, there are many difficulties in obtaining accurate measurements from these ablated companions. Even when using a model of an irradiated companion, the short timescale variability, the unevenly heated surface,

and the observed asymmetry in the light curves significantly hinder the orbital inclination measurements. Similarly, the difference between the center of light of the irradiated companion and its center of mass as well as the departure of the spectral features from assumptions of thermodynamic equilibrium introduce large uncertainties in the inferred mass ratios (Roberts et al. 2014). These results are tantalizing and hint at the possibility of even more massive NSs than J0348+0432, but because of the systematics, we find that they are not yet as robust as the results from radio timing.

3. RADIUS MEASUREMENTS

NS radius measurements have progressed significantly in the past decade and a number of different techniques have been employed. Nearly all of the methods that are currently used rely on the detection of thermal emission from the surface of the star either to measure its apparent angular size or to detect the effects of the NS spacetime on this emission to extract the radius information. The approaches can broadly be divided into spectroscopic and timing measurements. In addition, there are proposed methods for determining NS radii that show promise for the future but are not covered in this review, because there are currently limited data or because they provide only broad limits:

1. Quasi-periodic oscillations observed from accreting NSs (e.g., Miller et al. 1998),
2. NS cooling (e.g., Page & Reddy 2006),
3. Pulsar glitches, which help constrain the relative thicknesses of NS crust versus its core (e.g., Link et al. 1999), and
4. Asteroseismology (e.g., Watts et al. 2016).

3.1. Spectroscopic Measurements

Much like measuring the radii of normal stars, spectroscopic measurements of NS radii rely on determining their angular sizes by measuring a thermal flux F, modeling the spectrum to determine the effective temperature $T_{\rm eff}$, and combining this with a distance measurement D to obtain observed (or apparent) radii

$$\frac{R_{\rm obs}}{D} = \left(\frac{F_{\rm bol}}{\sigma_{\rm B} T_{\rm eff}}\right)^{1/2}, \tag{9}$$

where $\sigma_{\rm B}$ is the Stefan-Boltzmann constant. Unlike stars, however, there are several complications that come into play in this process. First, owing to their extreme compactness, NSs gravitationally lens their own surface emission. This introduces mass-dependent corrections to the observed angular sizes (Pechenick et al. 1983, Psaltis et al. 2000), i.e., the physical radii are related to the observed radii via

$$R_{\rm obs} = \left(1 - \frac{2GM}{Rc^2}\right)^{-1/2} R. \tag{10}$$

(This equation holds as long as the radius is larger than the photon orbit $3GM/c^2$. If it is smaller, then the geometric radius observed at infinity would be equal to $\sqrt{27}GM/c^2$, independent of the stellar radius.) The situation is even more complex in the case of NSs that spin moderately fast, because their spacetime can no longer be described by a Schwarzschild metric, and there are further spin-dependent corrections to the observed angular sizes (Bauböck et al. 2015). Second, the surface emission may be contaminated by nonthermal emission from an isolated NS's magnetosphere or by the disk surrounding an accreting one. Third, the magnetic field an NS possesses can be strong enough to cause temperature nonuniformity on the surface, which complicates the inference of

the true stellar radius. Fourth, distances to NSs are, in general, more difficult to measure than those to normal stars.

Some of these challenges are overcome by detailed theoretical modeling of emission from NSs in GR. Others are mitigated or eliminated by careful source selection (e.g., sources with low magnetic fields, with low accretion luminosities, or located in GCs with known distances) and by combining multiple observational phenomena to break the inherent degeneracies between NS mass and radius and to reduce the measurement uncertainties. With these criteria as a guide, thermal emission from LMXBs in quiescence and during X-ray bursts have been the focus of recent work on NS radii.

3.1.1. Quiescent low-mass X-ray binaries. The first group of sources on which radius measurement efforts have focused are the accreting NSs in LMXBs when they are in quiescence (qLMXBs). In quiescence, accretion ceases or continues at an extremely low level. This allows observations of the thermal emission from the stellar surface, which is powered by the reradiation of the heat stored in the deep crust during the accretion phases (Brown et al. 1998). Because of the short (~minutes) settling time of heavier elements in the surface layers of NSs (Brown et al. 2002), the atmospheres of NSs in quiescence are expected to be composed of hydrogen. (There are cases where the companion is hydrogen poor and a helium atmosphere may be appropriate; see below). The observed spectra of qLMXBs are indeed quasi-thermal, with a weak power-law component at high energies that is likely due to residual accretion.

A number of qLMXBs in GCs have been observed with the *Chandra X-Ray Observatory* and the *X-Ray Multi-Mirror Mission-Newton* (XMM-Newton). Their luminosities in quiescence are of the order of 10^{32-33} erg s^{-1}, making them very faint objects. In addition, the GC environments entail crowded fields. Because of this, the high angular resolution and low background of the modern X-ray instruments were crucial for obtaining spectroscopic constraints of their apparent angular sizes (e.g., Rutledge et al. 2001, Heinke et al. 2006, Webb & Barret 2007).

To make quantitative measurements from the observed spectra, radiative equilibrium models of NS atmospheres (Zavlin et al. 1996, Heinke et al. 2006) have been developed for a variety of surface compositions, surface gravities, and temperatures (for a recent review, see Özel 2013). Owing to the low magnetic field strengths of NSs in LMXBs (Psaltis & Chakrabarty 1999, and references therein), and the expectation of hydrogen atmospheres, unmagnetized hydrogen models have primarily been used in the spectral analyses to obtain observed angular sizes.

To date, reliable radius constraints have been obtained for eight qLMXBs located in the GCs M13, M28, M30, ω Cen, NGC 6304, and NGC 6397, and two in 47 Tuc (Heinke et al. 2006, Webb & Barret 2007, Guillot et al. 2011, Bogdanov et al. 2016). The observed (apparent) angular sizes obtained for these sources have been combined with GC distances (Harris 1996, Guillot & Rutledge 2014, Heinke et al. 2014) to measure their apparent radii. Under somewhat different assumptions, there have been several combined analyses of these measurements (Guillot et al. 2013, Guillot & Rutledge 2014, Lattimer & Steiner 2014, Özel et al. 2016). The most recent results are displayed as correlated contours on the NS M-R diagram (see **Figure 4**). (The full M-R likelihoods and tabular data for these sources can be found at **http://xtreme.as.arizona.edu/NeutronStars**.)

Several sources of systematic uncertainties that can affect the radius measurements have been studied. We discuss these in some detail below.

3.1.1.1. Atmospheric composition. The majority of qLMXBs for which optical spectra have been obtained show evidence for Hα emission (Heinke et al. 2014), indicating a hydrogen-rich companion. Although none of these spectra have been obtained for GC qLMXBs, assuming that sources in GCs have similar companions to those in the field led to the use of hydrogen atmospheres when

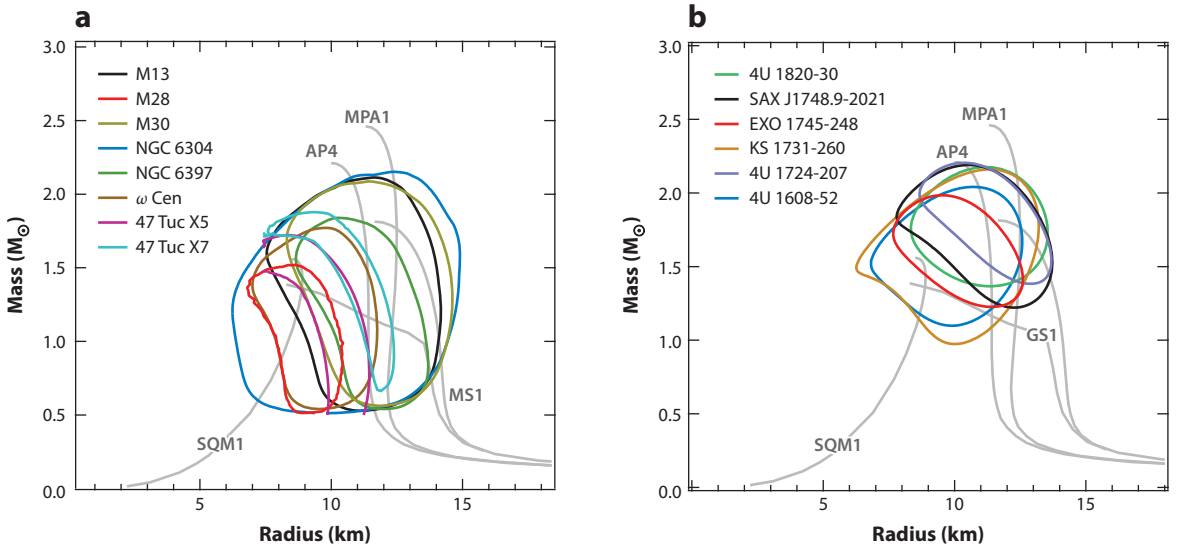

Figure 4

The combined constraints at the 68% C.L. over the neutron-star mass and radius obtained from (*a*) all neutron stars in low-mass X-ray binaries during quiescence and (*b*) all neutron stars with thermonuclear bursts. The light gray lines show mass relations corresponding to a few representative EoSs (see Section 4.1 and **Figure 7** for detailed descriptions and the naming conventions for all equations of state).

modeling quiescent spectra. There is one source among the six that have been analyzed in detail, for which there is evidence to the contrary. There is only an upper limit on the Hα emission from the qLMXB in NGC 6397 using *Hubble Space Telescope* observations (Heinke et al. 2014). Because of this, this source has been modeled with a helium atmosphere and the corresponding results are displayed in **Figure 4**.

3.1.1.2. Nonthermal component. Assuming different spectral indices in modeling the nonthermal spectral component also has a small effect on the inferred radii (Heinke et al. 2014). The low counts in the spectra do not allow an accurate measurement of this parameter; however, a range of values have been explored in fitting the data.

3.1.1.3. Interstellar extinction. Because of the low temperature of the surface emission from qLMXBs, the uncertainty in the interstellar extinction has a nonnegligible effect on the spectral analyses. Different amounts of interstellar extinction have been assumed in different studies (Guillot et al. 2013, Lattimer & Steiner 2014). A recent study explored different models for the interstellar extinction in the analysis of the qLMXBs in ω Cen and NGC 6397 and found statistically consistent results with small differences in the central values but larger differences in the uncertainties (Heinke et al. 2014). The relevant uncertainties have been incorporated into the results shown in **Figure 4**.

3.1.2. Thermonuclear bursts. NSs in LMXBs show a phenomenon called thermonuclear (Type-I) X-ray bursts, in which the accreted material undergoes a helium flash that consumes the fuel that is spread over the NS surface. The observed X-ray luminosity rises rapidly, in a timescale of $\approx$1 s, which corresponds to the diffusion timescale from the burning layer to the

NS surface. The energy is then radiated away on a timescale of ∼15–50 s for the majority of bursts during the so-called cooling tails. In a subset of the cases, the luminosity reaches the Eddington luminosity where the radiation forces match or exceed the gravitational forces and lift the photosphere off of the NS surface. These photospheric radius expansion (PRE) events have characteristic signatures in which the photosphere is observed to reach several times the NS radius and the temperature has a second rise (Lewin et al. 1993).

Several approaches have been developed and used to determine the NS radius by making use of thermonuclear bursts. Van Paradijs (1979) introduced using the apparent angular size obtained during the cooling tails of the bursts as a way to obtain correlated M-R constraints. Subsequently, Fujimoto & Taam (1986), Sztajno et al. (1987), Damen et al. (1990), and Özel (2006) discussed different ways in which the degeneracy between the radius and the mass can be broken through multiple spectroscopic measurements.

Özel & Psaltis (2009), Güver et al. (2010a), and a number of studies since have used a combination of the apparent angular sizes, the Eddington fluxes obtained from the PRE bursts, and the source distances to measure the NS radius and mass. In particular, the apparent angular sizes were measured from the flux and the temperature obtained from time-resolved spectroscopy, whereas the Eddington limit is measured at the moment when the photosphere touches back down onto the stellar surface. The Eddington flux is related to stellar parameters M and R and distance D via

$$F_{\rm Edd} = \frac{GMc}{k_{\rm es} D^2} \left(1 - \frac{2GM}{Rc^2}\right)^{1/2}, \tag{11}$$

where

$$k_{\rm es} \equiv 0.2(1+X) \left[1 + \left(\frac{kT_c}{38.8\ {\rm keV}}\right)^{a_g} \left(1 - \frac{2GM}{Rc^2}\right)^{-a_g/2}\right]^{-1} \ {\rm cm^2\ g^{-1}} \tag{12}$$

is the electron scattering opacity, and the last term in the equation arises from temperature corrections to electron scattering (Paczynski 1983, Suleimanov et al. 2012). X is the hydrogen mass fraction of the atmosphere,

$$a_g = 1.01 + 0.067 \left(\frac{g_{\rm eff}}{10^{14}\ {\rm cm\ s^{-2}}}\right), \tag{13}$$

and the effective surface gravity is given by

$$g_{\rm eff} = \frac{GM}{R^2} \left(1 - \frac{2GM}{Rc^2}\right)^{-1/2}. \tag{14}$$

Because the dependence of the Eddington flux on the stellar mass and radius (Equation 11) is different from that of the apparent angular size (Equation 10), combining these two spectroscopic measurements breaks the degeneracies between the stellar parameters introduced by GR effects.

Atmosphere models during bursts are used for the interpretation of spectra and the correct measurement of effective temperatures. A number of such models have been developed, addressing the Comptonization of photons by the hot surface electrons with increasing levels of sophistication and have been calculated for a range of surface compositions and effective gravities (London et al. 1986, Madej et al. 2004, Majczyna et al. 2005, Suleimanov et al. 2012). The deviations from a blackbody at the effective temperature of the atmosphere are quantified by the so-called color correction factor $f_c = T_{\rm c}/T_{\rm eff}$, which is then folded into these measurements.

Finally, the measured angular sizes are subject to additional general relativistic corrections due to moderately high spin frequencies observed in NSs with thermonuclear bursts. In particular, the effects of the quadrupole moment and the ellipticity of the NS on the NS spacetime as well as the

rotational broadening of the thermal spectra can be calculated in the Hartle-Thorne metric and lead to corrections in the inferred angular size of the order of ∼10% (Bauböck et al. 2015).

This approach has been applied to the NSs in the LMXBs EXO 1745−248 (Özel & Psaltis 2009), 4U 1820−30 (Güver et al. 2010a), 4U 1608−52 (Güver et al. 2010b), KS 1731−260 (Özel et al. 2012a), SAX J1748.9−2021 (Güver & Özel 2013), and 4U 1724−207 (Özel et al. 2016). Özel et al. (2016) performed an updated analysis with several improvements, using new statistical methods (Özel & Psaltis 2015) and applying the theoretical corrections discussed above, and uniformly incorporated systematic uncertainties into the measurements. The resulting 68%-C.L. contours over the mass and radius for these six NSs are shown in **Figure 4**. When combined, these measurements indicate NS radii in the 9.8–11-km range, which is consistent with the results obtained from the analyses of qLMXBs.

Another approach that has been utilized for radius measurements is to determine the spectral evolution of the color correction factor in PRE bursts (see Majczyna & Madej 2005 , Suleimanov et al. 2011, Poutanen et al. 2014). Because the spectral distortions depend on the effective surface gravity $g_{\rm eff}$ and the emitted flux, the change in the color correction factor with luminosity as the burst cools down from an Eddington flux can provide a measure of the stellar mass and radius. The application of this method to 4U 1728−34 (Majczyna et al. 2005), 4U 1724−207 (Suleimanov et al. 2011), 4U 1608−52 (Poutanen et al. 2014), and recently three additional sources (Nättilä et al. 2016) led to radii measurements that range from very small ($R < 6$ km in the case of 4U 1728–34) to quite large (13 km $< R <$ 16 km for 4U 1608−52). The data selection used in the latter studies is discussed below.

One final approach is to compare the observed properties of the bursts, such as their recurrence and decay times, and their peak fluxes to the expectations from theoretical light curve models to infer a surface redshift for the NS. These constraints can then be combined with the spectral evolution during the burst cooling tails to obtain constraints on the NS radius. Unfortunately, the theoretical models in this case are not very predictive and fail to explain the light curves of almost any of the nearly 50 sources extensively studied with the *Rossi X-Ray Timing Explorer* (Heger et al. 2007, Galloway et al. 2008). Therefore, the application of this method has been limited to the one source, GS 1826−24, where models can approximately match the light curve properties, and resulted in the limits $R < 6.8$–11.3 km for $M < 1.2$–1.7 $M_\odot$ (Zamfir et al. 2012), which is also consistent with the results obtained from qLMXBs and with PRE bursts (see **Figure 4**).

As with the qLMXBs in GCs, several sources of systematic uncertainty exist in the spectroscopic measurements of thermonuclear bursts. Their effects on the radius measurements have been studied in recent years, and these are discussed in some detail below.

3.1.2.1. Distances. Two of the three techniques discussed above rely on a measurement of source distances to obtain NS radii. For the sources that reside in GCs, the cluster distances are utilized. These are subject to the same uncertainties as those used for the qLMXB measurements. Other techniques have also been considered to measure distances to bursting NSs (Kuulkers et al. 2003, Güver et al. 2010a, Özel et al. 2012a). In most cases, these measurement techniques yield either reliable lower limits or source distances with relatively large uncertainties, which dominate the resulting uncertainties in the radius measurements.

3.1.2.2. Detection of outliers. As with all physical measurements, identification of outliers in data sets that may contaminate the results is an important issue. Güver et al. (2012a,b) developed a data-driven Bayesian Gaussian-mixture approach to identify the outliers in the spectroscopic burst data without any theoretical biases. The resulting selected data were used in the radius measurements reported by Özel et al. (2016). In an alternative approach, Poutanen et al. (2014) and Kajava et al.

(2014) performed data selection by requiring that the observations follow theoretical expectations. This approach resulted in a selection of a different, and much smaller, subset of bursts and led to the measurement of a stellar radius $R > 12$ km for 4U 1608−52 and to 10.5 km $< R <$ 12.8 km for the three sources used by Nättilä et al. (2016). The consistency of the burst evolution with theoretical expectations and the limitations of the latter method when applied to *Rossi X-Ray Timing Explorer* data are discussed in detail by Özel et al. (2015).

3.2. Radii via Pulse Profile Modeling

NS radii can also be measured or constrained by analyzing the properties of periodic brightness oscillations originating from temperature anisotropies on the surface of a spinning NS. The amplitudes and the spectra of the oscillation waveforms depend on the NS spacetime, which determines the strength of the gravitational light bending the photons' experience as they propagate to an observer at infinity (Pechenick et al. 1983), as well as on the temperature profile on the stellar surface and on the beaming of the emerging radiation. Using theoretical models for the emerging radiation, the properties of the brightness oscillation can, therefore, be used to probe the stellar spacetime and to measure its radius and mass.

The theoretical work on NS spacetimes has enabled increasingly more precise calculations of the effects of the gravitational lensing on the surface photons, which are used for the analyses of the waveforms. Earlier approximations appropriate for nonspinning NSs (Pechenick et al. 1983) were supplemented by adding in the effects of Doppler shifts and aberration (Miller & Lamb 1998, Muno et al. 2002, Poutanen & Beloborodov 2006) or those of frame dragging (Braje et al. 2000) for slow spins up to 300 Hz. At even faster spins, the oblateness of the NS and the quadrupole moment of its spacetime on the photon trajectories have been accurately accounted for (Morsink et al. 2007, Psaltis & Özel 2014). For stars near break-up (>1 kHz), fully numerical solutions of the spacetimes become necessary (Cook et al. 1994, Stergioulas & Friedman 1995, Cadeau et al. 2007).

The waveforms depend also on the location and the size of the hot spots, the beaming pattern of the radiation emitted from the stellar surface and the line of sight of the observer with respect to the rotation axis. Modeling the shapes and amplitudes of the waveforms, therefore, can yield constraints on a combination of all of these parameters and result in measurements of these parameters with correlated uncertainties. The challenge here is to reduce the number of unknowns and to eliminate the correlated uncertainties between the parameters in order to obtain a measurement of the NS radius. The size of the hot spot has a minor effect when it is sufficiently small (Bauböck et al. 2015), so this parameter can be eliminated in some cases. The beaming of radiation can also be calculated from atmosphere models.

Analysis of the oscillation waveforms has been performed to explore the properties of numerous types of NSs. Although this method yielded useful results on the surface emission properties of slow pulsars (Page 1995) and magnetars (DeDeo et al. 2001, Özel 2001), constraints on the NS radius and spacetime come, in particular, from the analysis of oscillations from accretion-powered MSPs, rotation-powered MSPs, and thermonuclear X-ray bursters. These three classes have distributions of spin frequencies that differ from one another, as shown in **Figure 5**. Therefore, spin effects need to be incorporated to different levels when modeling each population. We discuss the radius measurements from each of these classes individually below.

3.2.1. Rotation-powered pulsars. Even though the emission from rotation-powered MSPs is largely nonthermal and is dominated by their magnetospheres, a number of sources show a clearly detected thermal component in the soft X-rays (see, e.g., Grindlay et al. 2002; Bogdanov et al. 2006;

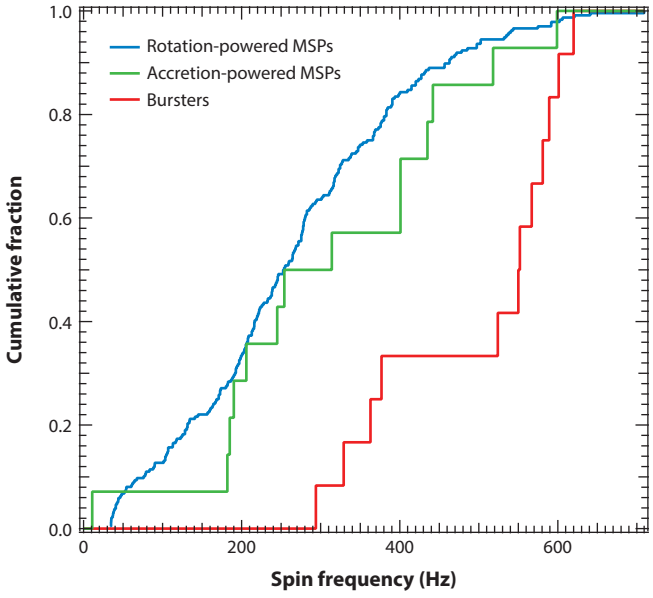

Figure 5

The cumulative distribution of spin frequencies of rotation-powered millisecond pulsars (MSPs), accretion-powered MSPs, and accreting neutron stars that show thermonuclear burst oscillations.

Zavlin 2006, 2007). X-ray data from a number of MSPs, obtained with *Röntgensatellit* (ROSAT), *Chandra X-Ray Observatory*, and XMM-Newton, have been analyzed using hydrogen atmosphere models for the thermal emission from a polar cap (see, e.g., Zavlin & Pavlov 1998). In these models, pulse profiles are calculated based on the beaming of radiation predicted by the theoretical models (see Özel 2013 for details).

An analysis of PSR J0437−4715, assuming a mass of 1.4 $M_\odot$, yielded bounds on the radius in the $R = 6.8$–13.8-km range (90% C.L.; Bogdanov et al. 2007). A subsequent measurement of the pulsar mass at 1.76 $M_\odot$ (Verbiest et al. 2008) increased the lower limit on the NS radius to $R > 11.1$ km (99.9% C.L.; see **Figure 6** and Bogdanov 2013), but this result is likely to be revised again in view of the most recent measurement of the pulsar mass (see **Table 2**). Similar analyses for PSRs J0030+0451 and J2124−3358 lead to lower limits on their radii of 10.7 km (95% C.L.) and 7.8 km (68% C.L.), respectively, assuming a pulsar mass of 1.4 $M_\odot$.

There are a number of complexities that affect the interpretation of the pulsar waveform data from MSPs. First, the nonthermal magnetospheric emission is subtracted from the total observed emission in the X-rays to allow for modeling of the thermal surface component from the polar caps. The thermal component itself is typically modeled with two separate regions with different temperatures, each emitting with a hydrogen atmosphere spectrum (Zavlin 2006, Bogdanov et al. 2007). The pulse profiles have been modeled with two polar caps, but the waveforms have required a nonantipodal geometry and led to additional uncertainties from introducing an additional offset parameter. The footprints of polar caps in the studies performed to date have assumed circular caps, but the effect of the shape of the polar cap on the waveforms has not yet been explored (see, however, Bauböck et al. 2015 for the effect of the unknown shape and size of the polar caps). Finally, the angles that specify the observer's line of sight and the colatitude of the polar caps with respect to the stellar spin axis are assumed to be known independently. The uncertainties introduced by the errors in these angles have not been factored into the quoted radius constraints.

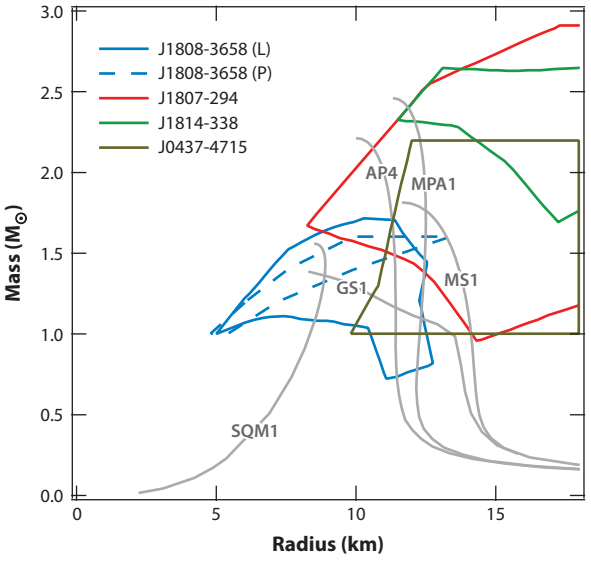

Figure 6

The radii constraints obtained from analysis of the waveforms from accretion-powered (Poutanen & Gierliński 2003; Leahy et al. 2008, 2009, 2011) and rotation-powered millisecond pulsars (Bogdanov 2013). Two different analyses of the SAX J1808.4−3658 data by Poutanen et al. (2003; denoted by P) and Leahy et al. (2008; denoted by L) are included.

Future work is needed to assess the effects of these assumptions and to quantify the additional resulting uncertainties in the radius measurements.

3.2.2. Accretion-powered pulsars. Thermal emission is observed in a number of accretion-powered millisecond X-ray pulsars (AMSPs) in the soft X-rays. It originates from the base of the accretion column, which is then Comptonized in that column (see Poutanen & Gierlinski 2003, their section 3.3).

A number of studies have modeled the emission from the X-ray-emitting regions at the bases of the accretion columns (Poutanen & Gierliński 2003, Lamb et al. 2009). The thermal photons emitted from the surface are Compton scattered in the accretion column, affecting the observed pulse amplitudes. Lamb et al. (2009) also explored the effect of the location of the X-ray-emitting regions and considered models in which the base of the accretion column wobbles around the spin axes. These models help interpret the AMSP timing data but also explore uncertainties in the M-R constraints obtained from fitting the waveforms.

This method has been applied to several AMSPs: SAX J1808.4−3658 (Poutanen & Gierliński 2003, Leahy et al. 2008, Morsink & Leahy 2011), XTE J1807−294 (Leahy et al. 2011), and XTE J1814−338 (Leahy et al. 2009). **Figure 6** shows the inferred constraints on the mass and radius of the NSs in these studies, where the contours depict 99% C.L. The large uncertainties in the M-R measurements shown in this figure reflect the influence of the various geometric factors discussed above, which are difficult to constrain.

3.2.3. Thermonuclear burst oscillations. Periodic flux oscillations with large amplitudes originating from the surfaces of NSs have also been detected during thermonuclear X-ray bursts

(Strohmayer et al. 1996). They originate from temperature nonuniformities on the stellar surface that occur during the nuclear burning (see Watts 2012 for a review). Modeling the pulse profiles of these burst oscillations is also a good probe of the stellar gravity and leads to constraints on the NS compactness (Strohmayer et al. 1997, Miller et al. 1998). In particular, the amplitude of the oscillations, the deviations from a sinusoidal waveform, and their dependence on photon energy can be probes of the NS radius and mass (Weinberg et al. 2001; Muno et al. 2002, 2003).

This technique was applied to oscillations observed from 4U 1636−536 (Nath et al. 2002) but led to no significant constraints on the NS radius or compactness. For the NS in XTE J1814−338, the analysis of the waveforms (e.g., Lo et al. 2013) of burst oscillations resulted in the limit on the NS compactness $R/M > 4.2$ (Bhattacharyya et al. 2005). Future observations can make use of more properties of the observed waveforms, such as their energy dependence and the amplitudes of the higher harmonics (Psaltis et al. 2014); the prospects are more comprehensively discussed in Watts et al. (2016).

4. THE NEUTRON-STAR EQUATION OF STATE

In addition to characterizing NS populations as well as understanding their formation and evolution, one of the ultimate goals of M-R measurements is, of course, to constrain the ultradense matter EoS. The microphysics, as described by the EoS, is connected to the macroscopic properties of the NS via the Tolman-Oppenheimer-Volkoff (TOV) equations, which provide the direct relation that is necessary to use astrophysical observations to constrain nuclear physics at very high densities. In this section, we describe this relation, a variety of theoretical approaches to as well as the low-energy experimental constraints on the EoS, and the current measurement of the EoS beyond nuclear saturation density from NS observations.

4.1. Neutron-Star Structure

The structure of relativistic stars and their M-R relation are determined by integrating the relativistic structure equations, also known as the TOV equations (Oppenheimer & Volkoff 1939; Tolman 1934, 1939):

$$\begin{aligned}\frac{\mathrm{d}p}{\mathrm{d}r} &= -\frac{\mathrm{G}}{c^2}\frac{(p+\epsilon)(m+4\pi r^3 p/c^2)}{r^2[1-2\mathrm{G}m/(rc^2)]},\\ \frac{\mathrm{d}m}{\mathrm{d}r} &= 4\pi r^2\frac{\epsilon}{c^2}.\end{aligned} \tag{15}$$

Here, p is the pressure, ϵ is the energy density, r is the radius, and m is the enclosed mass from the center, $r = 0$, where $p = p_c$ and $\epsilon = \epsilon_c$ to the surface at $r = R$ (where $p = 0$ and the enclosed mass is equal to the total mass $m = M$). (At moderate spin frequencies $f_{\mathrm{NS}} \lesssim 800$ Hz, rotational corrections appear at a less-than-a-few-percent level; see Cook et al. 1994, Stergioulas & Friedman 1995.) To complete this set of equations, one needs to specify the pressure-energy density relation, referred to as the EoS, appropriate for NS matter.

Before we proceed with a discussion of the cold dense matter EoS, a few remarks on the relevant quantities and units are in order. Although the energy density ϵ enters the TOV equations, most nuclear EoS calculations also use or refer to the baryon number density n (in units of $\mathrm{fm}^{-3} \equiv 10^{39}\mathrm{cm}^{-3}$) or to the mass density ρ (in units of $\mathrm{g\,cm}^{-3}$). The nuclear saturation density can then be equivalently expressed as a mass density $\simeq 2.8\times10^{14}\,\mathrm{g\,cm}^{-3}$ or a particle density $\simeq 0.16\,\mathrm{fm}^{-3}$. Similarly, the pressure is typically expressed in units of MeV $\mathrm{fm}^{-3} \equiv 1.6\times10^{33}$ erg cm^{-3}.

In NS cores, matter is cold and ultradense, characterized by large chemical potentials and a significant asymmetry in the numbers of neutrons and protons. Indeed, the condition of β equilibrium, given by

$$\left(\frac{\partial \epsilon/n}{\partial Y_e}\right)_n = \mu_e + \mu_p - \mu_n = 0, \tag{16}$$

points to proton fractions of $x \lesssim 10\%$, which is unlike normal nuclei that possess nearly equal numbers of protons and neutrons (referred to as symmetric matter). In the equation above, ϵ/n is the energy per baryon; μ_e, μ_p, and μ_n are the chemical potentials of the electrons, protons, and neutrons, respectively; and Y_e is the number of electrons per baryon. The densities in the cores can reach $\sim 10\ \rho_{\rm sat}$. Given that neutrons geometrically overlap at $\sim 4\ \rho_{\rm sat}$, at these extreme densities, matter may not be composed of nucleons alone but may contain a rich variety of hadronic degrees of freedom. With increasing overlap between nucleons, transitions to nonnucleonic states of matter are expected. For example, a gradual onset of quark degrees of freedom and quark constituents propagating throughout the system become likely (e.g., Alford et al. 2005, Kojo et al. 2015). In addition, Bose-Einstein condensates of mesons, such as pion (Akmal et al. 1998, Pandharipande et al. 1995, Mukherjee 2009) or kaon condensates (Kaplan & Nelson 1986, Brown et al. 1992, Glendenning & Schaffner-Bielich 1999) can enter at higher densities. It is also possible for ultradense matter to contain strange quarks in forms other than kaons, as weak interactions in the cold NS cores can lead to states of matter with a high degree of strangeness. Some of the possibilities considered to date include the presence of hyperons (Ambartsumyan & Saakyan 1960, Glendenning & Moszkowski 1991, Schulze et al. 1995), hybrid stars containing free quarks (Collins & Perry 1975), or color superconducting phases (Alford & Reddy 2003, Alford et al. 2005). Moreover, self-bound stars consisting of strange quark matter (SQM) have also been proposed (Farhi & Jaffe 1984, Haensel et al. 1986, Alcock et al. 1986). These models are based on the assumption that SQM is the ultimate ground state of matter (Itoh 1970, Witten 1984), predicting stellar radii that grow with the stellar mass.

First principles are not yet able to describe the interactions of such a system at several times the nuclear saturation density (but there is significant recent progress in describing the quark matter EoS at even higher densities and extrapolating down to lower densities; see, e.g., the discussion and results in Kurkela et al. 2014 and Kojo et al. 2015). Because of that, a number of different approaches have been followed in the calculations of the EoS of NS matter. A comprehensive overview of the methods and the details of the nuclear physics are given by Glendenning (2000), Lattimer & Prakash (2001), and Baldo & Burgio (2012). Here, we provide a summary of the basic methods as well as a compilation of some representative model EoSs.

One common effective field theory–motivated approach relies on expanding the nuclear Hamiltonians into two-, three-, . . . N-body static potential terms, assuming that the forces between particles can be described via static few-body potentials. The two-body potential is determined in the vicinity of $\rho_{\rm sat}$ for symmetric matter using nucleon–nucleon scattering data below 350 MeV and the properties of light nuclei, and the contributions from the three-body potentials are added (Akmal et al. 1998, Morales et al. 2002, Hebeler et al. 2010, Gandolfi et al. 2012). The resulting EoSs are particularly sensitive to the three-nucleon interactions because of the near-cancellation between the kinetic term and the two-body term in these potentials. In addition, such expansions are not valid at $\rho \gg \rho_{\rm sat}$ because the parameter measuring the relative importance of three-and-higher-body forces is $\sim \rho/(2m_\pi)^3 \approx 0.35\ \rho/\rho_{\rm sat}$. In these approaches, it is also common to make use of nuclear Hamiltonians that are experimentally constrained for symmetric matter around nuclear density and express the energy per baryon at higher density and at higher neutron fraction

as a parametric expansion in terms of the ratio $u \equiv \rho/\rho_{\rm sat}$ and the neutron excess $1-2x$:

$$\frac{\epsilon(u,x)}{n} = -B + \frac{K_o}{18}(u-1)^2 + \frac{K'_o}{162}(u-1)^3 + S_2(u)(1-2x)^2. \quad (17)$$

In this expansion, $B \simeq 16$ MeV is the bulk binding energy of symmetric matter at nuclear saturation density, and K_o and K'_o are the nuclear incompressibility and skewness parameters, respectively, and we only show terms up to quadratic order. It is also customary to call the quadratic term in neutron excess the symmetry energy and express it in terms of two parameters S_v, the symmetry energy at nuclear density

$$S_v = S_2(1), \quad (18)$$

and L, which is related to the derivative of the symmetry energy with respect to density

$$L = 3u\left(\frac{{\rm d}S_2}{{\rm d}u}\right)_{u=1}. \quad (19)$$

Naturally, at high density and high neutron fraction, these approaches also enter a regime where the expansions are not valid.

Alternatives to this approach include one that is based on field-theoretical calculations of constituents interacting via meson exchange (Müller & Serot 1996). A third approach involves microscopic ab initio calculations based on the Brueckner-Hartree-Fock model (Baldo et al. 1997); relativistic counterpart, the Dirac-Brueckner-Hartree-Fock model (Müther et al. 1987); or its modifications using unconventional Skyrme forces (Goriely et al. 2010; see also Potekhin et al. 2013 for analytical representations based on this EoS).

Figure 7*a* shows a large sample of currently proposed EoSs, spanning a density range of $\sim$0.1–8 $\rho_{\rm sat}$. The wide range of pressures P predicted under different assumptions is indicative of the wide-open questions in physics in this regime. The acronyms and the references for the various EoSs are described by Read et al. (2009). We also include in this figure (*a*) the recent EoS labeled NJL (Kojo et al. 2015) based on a smooth interpolation in pressure versus baryon chemical potential of a nucleonic EoS (APR) at densities below $\sim\rho_{\rm sat}$ with a quark matter EoS at densities above $\sim$5–7 $\rho_{\rm sat}$, (*b*) the BSK EoS of Goriely et al. (2010) and Potekhin et al. (2013), and (*c*) the QMC EoS of Rikovska Stone et al. (2007).

The M-R relations corresponding to the EoSs in **Figure 7** are shown in panel *b*. The curves that do not reach the observed $\sim$2-$M_\odot$ mass limit are denoted in light gray in this figure. Also note that the astrophysically relevant parts of these curves lie above $\sim 1\ M_\odot$. An important characteristic of many of these curves is that the radius remains nearly constant for the astrophysically relevant range of masses. The notable exceptions are the self-bound strange stars (e.g., SQM), where the radius increases with increasing mass, and stars with condensates (e.g., GS1-2, GM, PS), where the radius decreases with mass past the point at which the central density reaches the critical point where the phase transition occurs. The M-R curves are also characterized by a maximum mass beyond which there are no stable solutions. In general, EoSs with relatively higher pressures at densities above $\sim 4\ \rho_{\rm sat}$ have higher maximum masses. The presence of nonnucleonic phases, such as hyperons or condensates, reduces the pressure (referred to as softening the EoS) and leads to smaller maximum masses.

In the remainder of this section, we discuss how NS masses and radii can be used to pin down the ultradense matter EoS, the methodologies developed toward this goal, and the current state of the measurements. However, we first briefly describe the constraints on the nuclear EoS at nuclear density from low-energy experiments.

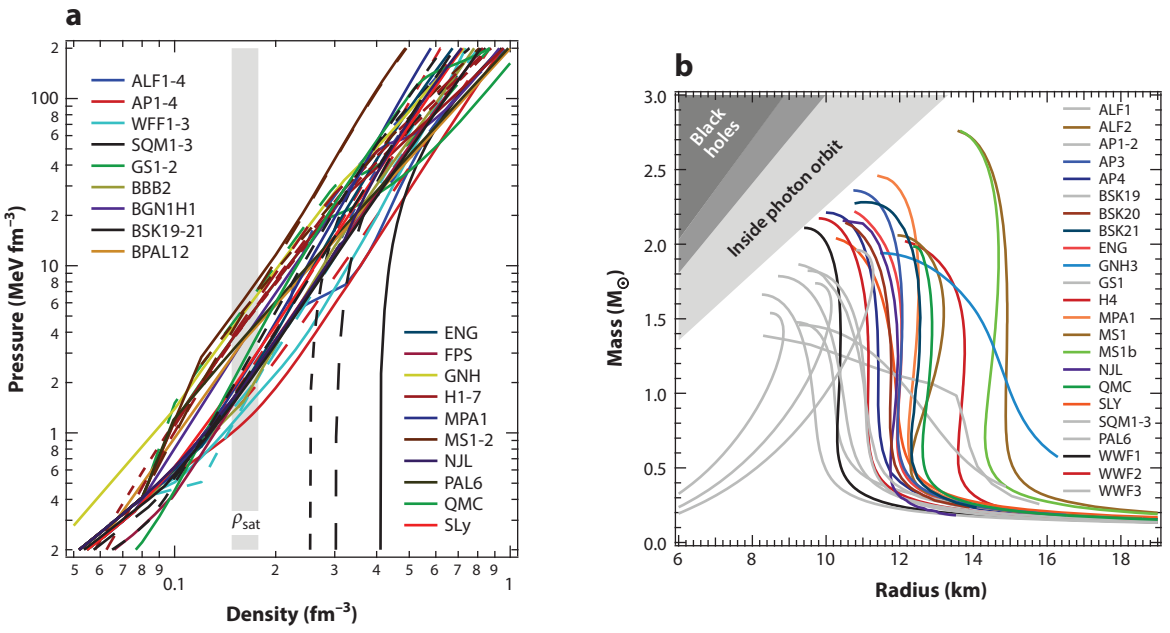

Figure 7

(*a*) A large sample of proposed EoSs calculated under different physical assumptions and using a range of computational approaches. See the text for the descriptions of the EoSs, the acronyms, and the references. (*b*) The mass-radius curves corresponding to the EoSs shown in panel *a*.

4.2. Constraints on the Equation of State from Low-Energy Experiments

For symmetric matter (i.e., nuclei containing roughly equal numbers of neutrons and protons) near the nuclear saturation density, there are a range of experimental constraints. Most robustly, two-body potentials can be inferred from nucleon–nucleon scattering data below 350 MeV and the properties of light nuclei (Akmal et al. 1998, Morales et al. 2002).

The other significant constraints that arise from these experiments and are relevant for the NS EoSs are often expressed in terms of the symmetry energy parameters: S_v and L (see Equations 18 and 19 in the previous section as well as the discussion in Lattimer 2012). The experiments that yield the most accurate data and the least model-dependent results involve fitting nuclear masses and charge radii (Klüpfel et al. 2009, Kortelainen et al. 2010). Nevertheless, the symmetry parameters that can be extracted from such data are highly correlated, as shown in **Figure 8**.

Neutron-rich matter can also be probed by measuring the neutron skin thickness of heavy nuclei. Studies within both the mean-field theory and the liquid droplet model frameworks have shown that the neutron skin thickness, defined as the difference of their neutron and proton root-mean-squared radii

$$\Delta r_{np} = \langle r_n^2 \rangle^{1/2} - \langle r_p^2 \rangle^{1/2}, \tag{20}$$

is a sensitive function of S_v and L and, thus, serves as a good probe of the symmetry energy (Centelles et al. 2009, Chen et al. 2010, Roca-Maza et al. 2011). The neutron skin thickness was measured by a variety of experiments for ≈20 neutron-rich Sn isotopes with ∼30–50% uncertainties. Chen et al. (2010) used these measurements to place additional constraints on the symmetry energy parameters (see **Figure 8**). In addition, the neutron skin thickness has been determined by

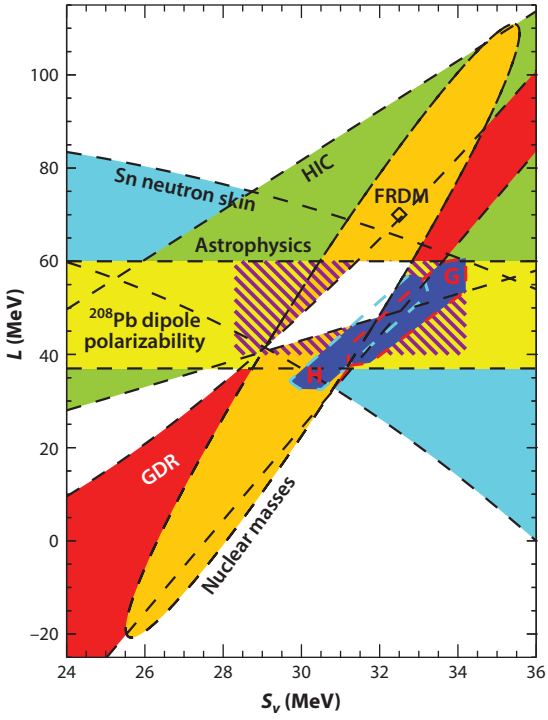

Figure 8

The experimental constraints on the symmetry energy parameters L and S_v from experiments performed near nuclear density. These include the neutron skin thickness of neutron-rich tin (Sn) isotopes (shown in *light blue*), giant dipole resonances (GDR, *red*), the dipole polarizability of ^{208}Pb (*light yellow*), and heavy-ion collisions (HIC, *green*) as well as nuclear masses (*dark yellow*, including the finite-range droplet model labeled FRDM). The theoretical inferences from Gandolfi (2012, denoted by G) and Hebeler (2010, denoted by H), as well as an earlier astrophysical inference from Lattimer (2012), are also indicated in this figure as dark blue and hatched regions, respectively. Reproduced with permission from Lattimer (2012).

the Lead Radius Experiment (PREX) for ^{208}Pb using a technique called parity-violating electron scattering (Abrahamyan et al. 2012): Because the weak-vector meson that mediates this interaction couples preferentially to neutrons, the approach allows a measurement of the neutron form factor, which can then be extrapolated to neutron skin thickness.

Another observable that places significant constraints on L comes from the measurement of the dipole polarizability of ^{208}Pb and the giant dipole resonances. The giant dipole resonance, measured from the response of the neutron-rich nuclei to an externally applied electric field, serves as a measure of the symmetry energy (Trippa et al. 2008, Tamii et al. 2011, Piekarewicz et al. 2012). The resulting constraints on S_v and L are also shown in **Figure 8**.

The most indirect experimental probe of the EoS of cold, neutron-rich, dense matter emerges from low-energy heavy-ion collisions. There are large uncertainties in extrapolating from the properties of hot dense matter generated in these collisions to zero temperature and to extreme neutron richness (Tsang et al. 2009). For completeness, **Figure 8** also includes these constraints.

Although these experiments are neither as powerful nor as direct probes of the NS EoS as a measurement of the macroscopic properties of NSs (as is shown in the next section), they serve as complementary tests of the properties of dense matter. At a minimum, the pressure obtained from the two-nucleon interaction serves as a lower limit to the pressure of NS matter at ∼1–2 ρ_{sat}. This is because three-body interactions in pure neutron matter are always repulsive. Considering the

expansion of the interaction in terms of two- and three-body potentials and using the contribution of the two-body potential (Argonne AV8 or AV18) yields a lower bound of $P = 7.56\,\mathrm{MeV\,fm^{-3}}$ at $\rho = 1.85\ \rho_{\mathrm{sat}}$ (Özel et al. 2016). This constraint has been used in conjunction with the NS radius measurements to determine the ultradense matter EoS, as we discuss in Section 4.4.

4.3. From Radius and Mass Measurements to the Neutron-Star Equation of State

Given the TOV equations, the EoS of NS matter determines the macroscopic properties of the stars and, in particular, their masses and radii. In fact, the solutions provide a unique map between the microscopic pressure-density relation [$P(\rho)$ or $P(\epsilon)$] and the macroscopic M-R relation of stars (Lindblom 1992).

This unique mapping can, in principle, be exploited to infer the EoS from astrophysical measurements of their masses and radii. However, a formal inversion of this mapping requires a measurement of the entire M-R curve, i.e., the measurement of radii for NSs that span the range of stellar masses between $\sim$0.2 $M_\odot$ and 2 $M_\odot$. This requirement severely limits the applicability of this direct inversion because there is no astrophysical formation channel for NSs with masses that are much smaller than the Chandrasekhar mass of the progenitor cores, and neither are such stars observed (see Section 2).

Despite this difficulty, the connection between the M-R relations and the EoS turns out to have certain characteristics that make it possible to infer them from a more sparse sampling of NS radii. In particular, the maximum mass is determined primarily by the behavior of the EoS at the highest densities ($\sim$7–8 ρ_{sat}; Özel & Psaltis 2009), whereas the radius depends primarily on the pressure at $\approx$2 ρ_{sat} (Lattimer & Prakash 2001). The slope of the M-R relation (i.e., whether R increases or decreases with M), in the mass range of astrophysical interest, depends largely on the pressure at $\sim$4 ρ_{sat} (Özel & Psaltis 2009). The fact that only a small number of densities determine the macroscopic properties of NSs means that their various higher-order moments cannot be completely independent from each other. Indeed, a number of universal relations have been found between various higher-order moments of NSs, such as the moment of inertia, the quadrupole moment, and the tidal Love number (Yagi & Yunes 2013, Bauböck et al. 2013, Yagi et al. 2014), the origins of which have not yet been fully understood.

These properties make it possible to infer the pressure of ultradense matter at a few appropriately chosen densities above ρ_{sat} instead of mapping out the full functional form of the EoS from astrophysical observations. The optimal densities for sampling and the parametric forms that lead to the smallest uncertainties in the EoS determination were explored in detail by Read et al. (2009) and Özel & Psaltis (2009). These studies showed that the pressures measured at 1.85 (P_1), 3.7 (P_2), and 7.4 ρ_{sat} (P_3) and connected by piecewise polynomials can represent more than forty proposed EoSs included in those studies to within a few percent uncertainty. These led to the realization that the measurement of the masses and radii of even a small number of NSs can provide significant input to the microphysics calculations, which was used in subsequent studies (Özel et al. 2010a, Steiner et al. 2010, Guillot & Rutledge 2014).

The mass of the heaviest NS measured to date can provide additional direct constraints on the EoS. At a minimum, the EoSs that have maximum masses that fall below the most massive NS can be ruled out (Demorest et al. 2010, Özel et al. 2010b, Antoniadis et al. 2013). However, more stringent constraints are achieved by combining the floor on the maximum mass with radius measurements (Steiner et al. 2010, Özel et al. 2016). Because the EoSs that produce smaller radii generally tend to have smaller maximum masses, combining these measurements yields smaller allowed confidence regions in the EoS parameters.

Bayesian techniques have been developed (Steiner et al. 2010, 2013; Özel et al. 2016) to combine radius measurements with the maximum mass constraint, as well as the data obtained from the low-energy experiments discussed in Section 4.2. These techniques yield likelihoods over the EoS parameters P_1, P_2, and P_3 from the M-R likelihoods $P(M_i, R_i)$ for i sources while allowing a variety of priors and other measurements to be incorporated (see Özel et al. 2016, and references therein for details).

The priors over P_1, P_2, and P_3 are then specified using numerous physical and observational constraints. First, for the EoS to be microscopically stable, it is necessary to require $P_3 \geq P_2 \geq P_1$ and that P_1 be greater than or equal to the pressure of matter at $\rho_0 = 10^{14}$ g cm^{-3} (see Özel & Psaltis 2009 for the particular specification using the SLy EoS). Second, for the EoS to be causal, the condition

$$c_s^2 = \frac{\partial P}{\partial \epsilon} \leq c^2, \tag{21}$$

where c_s is the sound speed and ϵ is the energy density, can be imposed at all densities. Third, to incorporate the mass requirement, the maximum stable mass for each EoS corresponding to a P_1, P_2, P_3 triplet needs to exceed 1.97 $M_\odot$, which is consistent within 1σ with the heaviest NSs observed to date.

The results from the laboratory experiments can be folded in as a requirement on the pressure at the lowest density P_1 or as constraints on the symmetry energy parameters L and S_v, which can be translated into constraints on P_i. As discussed in Section 4.2, the least model-dependent one of those requirements is a lower limit on $P_1 = 7.56$ MeV fm^{-3} such that the EoS is consistent with the most robust laboratory experiments and low-density calculations, i.e., with the APR EoS for pure neutron matter (Akmal et al. 1998). Finally, priors that are flat in log P_1, log P_2, and log P_3 or that are flat in P_1, P_2, and P_3 can be chosen. The sensitivity of the Bayesian inference of the EoS parameters on these conditions and priors is discussed by Steiner et al. (2013) and Özel et al. (2016).

4.4. Current Constraints on the Cold Neutron Matter Equation of State

In recent studies, the radius results summarized in Section 3 have been used in conjunction with the Bayesian parameter inference techniques to place strong constraints on the NS EoSs. The radius data include the fourteen sources shown in **Figure 4**. (Note that these omit the analysis of 4U 1724−207 by Suleimanov et al. 2011 and 4U 1608−52 by Poutanen et al. 2014, for which the data selection and analysis do not yield self-consistent results.)

Figure 9 shows the posterior likelihoods over the pressures at the three fiducial densities, as well as the microscopic and experimental bounds on these pressures. The pressures at the fiducial densities of a large number of proposed EoSs are also shown. The gray region labeled 2NI denotes the lower limit on P_1 coming from the two-body interaction potential obtained at low densities. P_1 is also constrained from above by the relatively small measured radii. Indeed, the values within the highest posterior likelihood are lower than the pressure predicted by most proposed EoSs at that density.

In contrast, the combination of P_2 and P_3 is constrained by the maximum mass requirement: a lower value of P_2 pushes P_3 to be as high as possible within the causality limit, whereas for moderate to high values of P_2, which already lead to M-R relations that allow high-mass stars and are consistent with the radius measurements, the allowed range of P_3 extends to lower values. The combination of P_2 and P_3 excludes to high confidence the stiff EoSs such as MPA1 and MS1, which produce radii that are too large (see also their inconsistency with P_1 in **Figure 9*b***). This

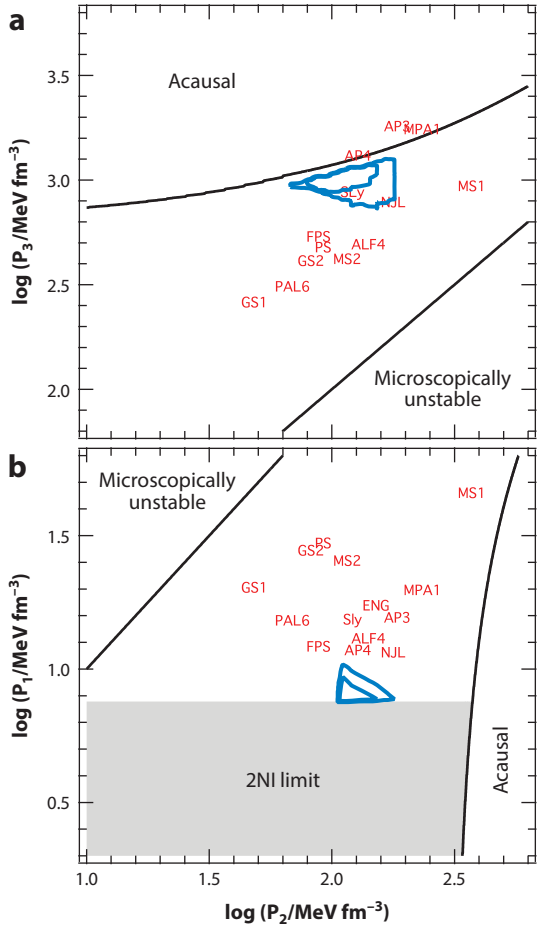

Figure 9

The highest likelihood regions in the pressure of neutron-star matter at 1.85 ρ_{ns} (P_1), 3.7 ρ_{ns} (P_2), and 7.4 ρ_{ns} (P_3) obtained by a parametric inversion of all the neutron-star radius measurements and requiring that the EoS is consistent with the maximum mass requirement and low-energy experiment data. To visualize the structure of the three-dimensional posterior likelihood function, the contours outline the regions in which the posterior likelihoods drop down to $e^{-1/2}$ and e^{-1} of the highest values. The allowed regions of the parameter space are consistent with the constraints from calculations based on low-energy scattering experiments, are microscopically stable, and ensure that the EoS remains causal. The gray region labeled 2NI denotes the lower limit on P_1 coming from the two-body interaction potential obtained at low densities.

combination also excludes EoSs with condensates, such as GS1, with pressures that are too low to be consistent with the maximum mass requirement.

Figure 9 shows that the combination of the radius measurements with the low-density experimental data and the requirement of a ~2-$M_\odot$ maximum mass pins down the parameters of the EoS extremely well across a wide range of supranuclear densities and points to a preferred EoS that is somewhat softer than the nuclear EoS AP4 (a version of the APR EoS). To see this on the M-R diagram, we also show in **Figure 10** the M-R relation corresponding to the most likely triplet of pressures as well as the range of M-R relations for the region of the (P_1, P_2, P_3) parameter space with the highest likelihood. We limit the range of masses in this figure to $\leq$2.2 $M_\odot$

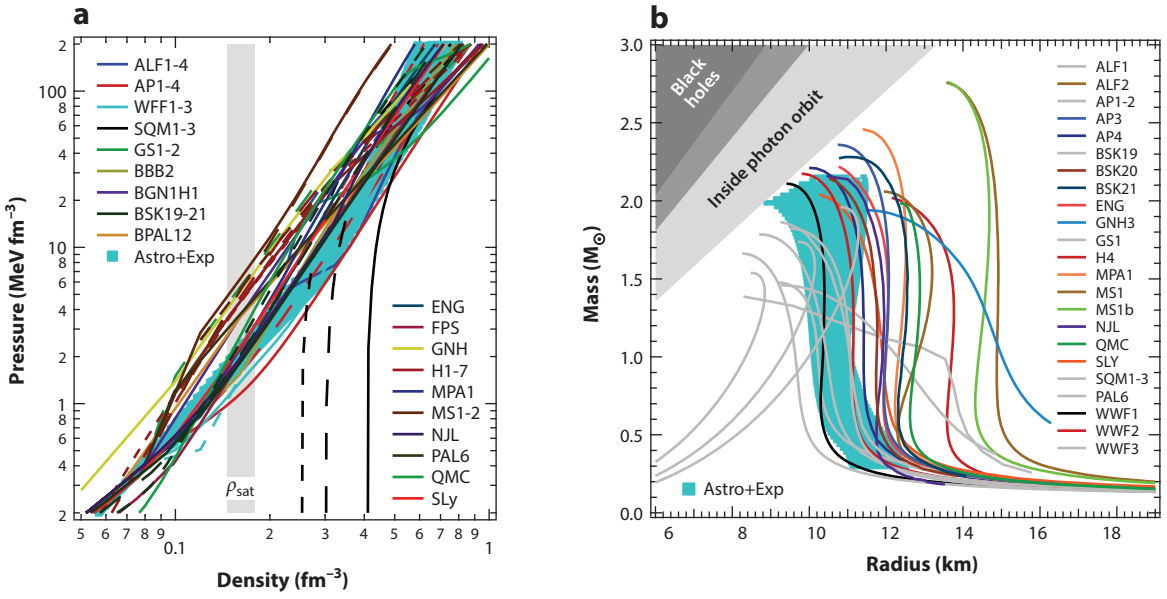

Figure 10

The astrophysically inferred (*a*) EoS and (*b*) mass-radius (M-R) relation corresponding to the most likely triplets of pressures that agree with all of the neutron-star radius and low-energy nucleon–nucleon scattering data and allow for an $M > 1.97$-M$_\odot$ neutron-star mass. The light blue bands show the range of pressures and the M-R relations that correspond to the region of the (P_1, P_2, P_3) parameter space in which the likelihood is within e^{-1} of its highest value. Around 1.5 M$_\odot$, this inferred EoS predicts radii in the range of 9.9–11.2 km.

because of the absence of any data to constrain the relation at higher masses. As expected from the above discussion, the preferred M-R relation lies to the left of most model predictions and is closest to AP4, especially at low masses, where the main uncertainty in AP4 is in the strength of the three-nucleon interactions. It also rises along a nearly constant radius in order to reach the ∼2-M$_\odot$ limit. Depending on the choice of the prior, the predicted radius for a 1.5-M$_\odot$ NS is between 10 and 11.5 km.

5. FUTURE PROSPECTS

5.1. The Future of Radio Pulsar Mass Measurements: New Surveys, New Binary Systems, New Measurements, and the Square Kilometre Array

We can expect the number of mass measurements to increase at an accelerating rate over the next few years. The reason for this is that improvements in instrumentation, in terms of both new receivers and the equipment used to detect and process the radio signals, are revolutionizing the field of pulsar timing and searching.

More sensitive receivers with larger bandwidths and the advent of broadband coherent dedispersion allow much more precise timing of the known binary pulsars. This leads to more precise measurements of known PK parameters and the detection of new ones, greatly increasing the sample of NS mass measurements and the number of GR tests in different systems. Furthermore, improved receiver sensitivities and larger bandwidth, together with multibeaming, increase the general sensitivity to all sorts of pulsars, as in the case of the phenomenally successful Parkes

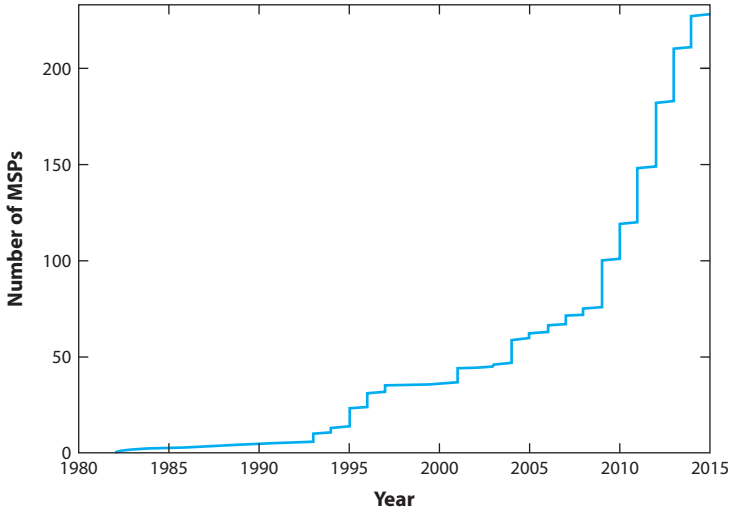

Figure 11

Number of millisecond pulsars (MSPs) (with $P < 20$ ms) known in the Galactic disk as a function of time. This figure does not take into account the more than 100 MSPs known in globular clusters. The large number of discoveries in recent years was enabled by improvements in the digital equipment being used in ground-based radio surveys and the discovery of many pulsar-like gamma-ray point sources by the *Fermi Gamma Ray Space Telescope*, which led to the discovery of many new radio MSPs. Data provided by Duncan Lorimer; see **http://astro.phys.wvu.edu/GalacticMSPs/GalacticMSPs.txt**.

multibeam (PMB) surveys (Manchester et al. 2001). Since then, the newer generation of post-PMB surveys like the new HTRU-South (Keith et al. 2010) and North surveys (Barr et al. 2013), the Green Bank drift scan survey (Boyles et al. 2013, Lynch et al. 2013), the Green Bank North Celestial Cap survey (Stovall et al. 2014), the Arecibo ALFA survey (Cordes et al. 2006, Lazarus 2013), and the Arecibo 327-MHz drift-scan survey (Deneva et al. 2013) has been making full use of much improved data-handling capabilities and processing power to obtain a large increase in spectral and time resolution (at a cost of 100 times the data rate). This has paid off with a great increase in the sensitivity to MSPs, particularly the distant ones, producing a great leap in their discovery rate. The number of discoveries per year is shown in **Figure 11**; we see a three-fold increase in the number of MSPs since 2010. This will continue for the next few years, as many of the new surveys are still starting. The rate of discovery will further accelerate as soon as the Square Kilometre Array (SKA) comes online (Kramer & Stappers 2014).

Not all these new MSPs were found in blind surveys. More than 100 were discovered in targeted radio searches of GCs (see **http://www.naic.edu/~pfreire/GCpsr.html**). This number is expected to increase to thousands with the SKA (Hessels et al. 2014). A new and very successful search strategy—with more than 60 new MSPs discovered at the time of writing—has been targeting unidentified pulsar-like gamma-ray sources discovered with the *Fermi Gamma Ray Space Telescope* (see, e.g., Ransom et al. 2011, Keith et al. 2011, Kerr et al. 2012). Apart from the intrinsic interest in discovering new MSPs, the gamma-ray pulsars are important in the sense that they are biased in favor of very short-period MSPs, which is the opposite of the outcome in normal blind surveys. This contributes to a better understanding of the underlying MSP population.

The large increase in the number of binary pulsars implies a large increase in the number of NS mass measurements and tests of GR, because discoveries of more edge-on systems will inevitably result from a larger MSP sample, as well as discoveries of more triples, eccentric MSP systems, and

DNSs. This trend is evident in **Tables 1** and **2**, where most of the reported results are relatively recent. Furthermore, the large sensitivity of planned radio telescopes such as the SKA will enable much improved timing precision of binary pulsars, new and old. This will further increase the number and precision of NS mass measurements and possibly allow a measurement of the upper mass limit for NSs.

5.2. The Future of Radius Measurements

The increase in the number of NS radius measurements and the continued reduction of the uncertainties will rely on a few factors. Distance uncertainties are currently one of the bottlenecks in the spectroscopic radius measurements. Therefore, one of the crucial improvements in this technique can come from obtaining distance measurements to many more NS X-ray binaries. The GAIA mission and radio parallax measurements may provide distances to the ones that are relatively nearby.

Radius measurements obtained by nonspectroscopic techniques, with potential biases and systematic uncertainties that are different than the spectroscopic ones, will be another key factor in verifying the current measurements. To this end, high signal-to-noise pulse profiles of rotation- and accretion-powered X-ray pulsars will provide a major step forward. Indeed, the technique of pulse profile modeling to measure the NS compactness and radii defines the key scientific objectives of several future X-ray missions, such as NASA's upcoming *Neutron Star Interior Composition Explorer Mission* (NICER; Gendreau et al. 2012), the Indian Space Research Organisation's ASTROSAT (Agrawal 2006), or the proposed *Large Observatory for X-Ray Timing* (Feroci et al. 2012) missions.

Among these missions, NICER, a NASA Mission of Opportunity, is poised to be launched to the International Space Station in 2017. NICER will collect a large number of counts from a small number of rotation-powered pulsars that emit thermally from their polar caps. In combination with the refined theoretical models that have been developed to analyze these waveforms, these data will provide a new measurement of NS radii and EoSs.

5.3. Other Future Probes of Neutron-Star Structure

The double pulsar will be the first system that will allow, in a few years, a measurement of the moment of inertia of an NS (Lyne et al. 2004, Kramer & Wex 2009). The moment of inertia, being a higher moment of the mass distribution of the NS, is a powerful probe of its internal structure and, hence, of its EoS (Morrison et al. 2004, Lattimer & Schutz 2005, Raithel et al. 2016).

There are also significant prospects for radius measurements from Advanced LIGO observations of coalescing NS binaries. The characteristic frequencies of these waveforms can be used to obtain information on the NS radius and deformability (see, e.g., Read et al. 2013), which will shrink the current uncertainties in the radius measurements and further constrain the dense matter EoS.

Finally, the EoSs of NSs can be inferred by measuring the total luminosity and the spectrum of neutrinos emitted during a core-collapse supernova explosion within our Galaxy.

FUTURE ISSUES

1. Continued measurements of NS masses will make the inferred NS mass distributions more robust and help constrain the maximum NS mass by increasing the size of the sample.

2. Comparing current radius measurements against those made with other techniques will further reduce the uncertainties in the NS radii.
3. Multimessenger probes such as gravitational waves, neutrinos, and moment-of-inertia measurements will open new avenues into NS structure.
4. Advances in lattice quantum chromodynamics will provide a first-principles calculation of the composition and interactions of the dense matter EoS, which can be compared with the results from NSs and laboratory experiments.
5. The hot dense matter EoS that is relevant to supernovae and NS mergers requires further study.

DISCLOSURE STATEMENT

The authors are not aware of any affiliations, memberships, funding, or financial holdings that might be perceived as affecting the objectivity of this review.

ACKNOWLEDGMENTS

We thank John Antoniadis, Michael Kramer, Ben Lackey, Jim Lattimer, Duncan Lorimer, Dimitrios Psaltis, Jocelyn Read, and Mallory Roberts for graciously providing materials for this review. We thank Gordon Baym, Tolga Guver, Ramesh Narayan, and Dimitrios Psaltis for numerous useful conversations and comments on the manuscript. F.Ö. gratefully acknowledges support from NSF grant AST 1108753. P.F. gratefully acknowledges financial support by the European Research Council for the ERC Starting grant BEACON under contract no. 279702.

LITERATURE CITED

Abdo AA, Ajello M, Allafort A, et al. 2013. *Ap. J. Suppl.* 208:17
Abrahamyan S, Ahmed Z, Albataineh H, et al. 2012. *Phys. Rev. Lett.* 108:112502
Agrawal PC. 2006. *Adv. Space Res.* 38:2989–94
Akmal A, Pandharipande VR, Ravenhall DG. 1998. *Phys. Rev. C* 58:1804–28
Alcock C, Farhi E, Olinto A. 1986. *Ap. J.* 310:261–72
Alford M, Braby M, Paris M, Reddy S. 2005. *Ap. J.* 629:969–78
Alford M, Reddy S. 2003. *Phys. Rev. D* 67:074024
Ambartsumyan VA, Saakyan GS. 1960. *Astron. Zh.* 37:193
Antoniadis J, Bassa CG, Wex N. 2011. *MNRAS* 412:580–84
Antoniadis J, Freire PCC, Wex N, et al. 2013. *Science* 340:448
Antoniadis J. Tauris TM Özel F, et al. 2016. *Ap. J.* Submitted. arXiv:1605.01665
Antoniadis J, van Kerkwijk MH, Koester D, et al. 2012. *MNRAS* 423:3316–27
Backer DC, Kulkarni SR, Heiles C, Davis MM, Goss WM. 1982. *Nature* 300:615–18
Bailes M. 2010. *New Astron. Rev.* 54:80–86
Baiotti L, Giacomazzo B, Rezzolla L. 2008. *Phys. Rev. D* 78:084033
Baldo M, Bombaci I, Burgio GF. 1997. *Astron. Astrophys.* 328:274–82
Baldo M, Burgio GF. 2012. *Rep. Prog. Phys.* 75:026301
Barr ED, Champion DJ, Kramer M, et al. 2013. *MNRAS* 435:2234–45
Bassa CG, van Kerkwijk MH, Koester D, Verbunt F. 2006. *Astron. Astrophys.* 456:295–304
Bauböck M, Berti E, Psaltis D, Özel F. 2013. *Ap. J.* 777:68
Bauböck M, Özel F, Psaltis D, Morsink SM. 2015. *Ap. J.* 799:22

Bauswein A, Janka HT, Hebeler K, Schwenk A. 2012. *Phys. Rev. D* 86:063001
Bégin S. 2003. *A search for fast pulsars in globular clusters*. MS thesis, Univ. Br. Columbia
Bhat NDR, Bailes M, Verbiest JPW. 2008. *Phys. Rev. D* 77:124017
Bhattacharyya S, Strohmayer TE, Miller MC, Markwardt CB. 2005. *Ap. J.* 619:483–91
Bogdanov S. 2013. *Ap. J.* 762:96
Bogdanov S, Grindlay JE, Rybicki GB. 2006. *Ap. J.l* 648:L55–58
Bogdanov S, Heinke C, Özel F, Güver T. 2016. *Ap. J.* Submitted. arXiv:1603.01630
Bogdanov S, Rybicki GB, Grindlay JE. 2007. *Ap. J.* 670:668–76
Boyles J, Lynch RS, Ransom SM, et al. 2013. *Ap. J.* 763:80
Braje TM, Romani RW, Rauch KP. 2000. *Ap. J.* 531:447–52
Brown EF, Bildsten L, Chang P. 2002. *Ap. J.* 574:920–29
Brown EF, Bildsten L, Rutledge RE. 1998. *Ap. J. Lett.* 504:L95–98
Brown GE, Kubodera K, Rho M, Thorsson V. 1992. *Phys. Lett. B* 291:355–62
Cadeau C, Morsink SM, Leahy D, Campbell SS. 2007. *Ap. J.* 654:458–69
Callanan PJ, Garnavich PM, Koester D. 1998. *MNRAS* 298:207–11
Camilo F, Kerr M, Ray PS, et al. 2015. *Ap. J.* 810:85
Caraveo PA. 2014. *Annu. Rev. Astron. Astrophys.* 52:211–50
Centelles M, Roca-Maza X, Viñas X, Warda M. 2009. *Phys. Rev. Lett.* 102:122502
Champion DJ, Lorimer DR, McLaughlin MA, et al. 2005. *MNRAS* 363:929–36
Champion DJ, Ransom SM, Lazarus P, et al. 2008. *Science* 320:1309–12
Chen LW, Ko CM, Li BA, Xu J. 2010. *Phys. Rev. C* 82:024321
Cocozza G, Ferraro FR, Possenti A, D'Amico N. 2006. *Ap. J. Lett.* 641:L129–32
Collins JC, Perry MJ. 1975. *Phys. Rev. Lett.* 34:1353–56
Cook GB, Shapiro SL, Teukolsky SA. 1994. *Ap. J.* 424:823–45
Cordes JM, Freire PCC, Lorimer DR, et al. 2006. *Ap. J.* 637:446–55
Corongiu A, Kramer M, Stappers BW, et al. 2007. *Astron. Astrophys.* 462:703–9
Damen E, Magnier E, Lewin WHG, et al. 1990. *Astron. Astrophys.* 237:103–9
Damour T. 2015. *Class. Quantum Gravity* 32:124009
Damour T, Deruelle N. 1985. *Ann. Inst. Henri Poincaré Phys. Théor.* 43(1):107–32
Damour T, Deruelle N. 1986. *Ann. Inst. Henri Poincaré Phys. Théor.* 44(3):263–92
Damour T, Esposito-Farèse G. 1996. *Phys. Rev. D* 54:1474–91
DeDeo S, Psaltis D, Narayan R. 2001. *Ap. J.* 559:346–52
Demorest PB, Pennucci T, Ransom SM, Roberts MSE, Hessels JWT. 2010. *Nature* 467:1081–83
Deneva JS, Stovall K, McLaughlin MA, et al. 2013. *Ap. J.* 775:51
Desvignes G, Caballero RN, Lentati L, et al. 2016. *MNRAS* 458:3341–80
Edwards RT, Bailes M. 2001. *Ap. J.* 553:801–8
Falanga M, Bozzo E, Lutovinov A, et al. 2015. *Astron. Astrophys.* 577:A130
Farhi E, Jaffe RL. 1984. *Phys. Rev. D* 30:2379–90
Ferdman RD, Stairs IH, Kramer M, et al. 2014. *MNRAS* 443:2183–96
Ferdman RD, Stairs IH, Kramer M, et al. 2010. *Ap. J.* 711:764–71
Feroci M, Stella L, van der Klis M, et al. 2012. *Exp. Astron.* 34:415–44
Fonseca E, Stairs IH, Thorsett SE. 2014. *Ap. J.* 787:82
Fonseca E, Pennucci TT, Ellis JA, et al. 2016. *Ap. J.* Submitted. arXiv:1603.00545
Freire PC, Camilo F, Kramer M, et al. 2003. *MNRAS* 340:1359–74
Freire PCC, Bassa CG, Wex N, et al. 2011. *MNRAS* 412:2763–80
Freire PCC, Ransom SM, Bégin S, et al. 2008a. *Ap. J.* 675:670–82
Freire PCC, Ransom SM, Gupta Y. 2007. *Ap. J.* 662:1177–82
Freire PCC, Wex N. 2010. *MNRAS* 409:199–212
Freire PCC, Wex N, Esposito-Farèse G, et al. 2012. *MNRAS* 423:3328–43
Freire PCC, Wolszczan A, van den Berg M, Hessels JWT. 2008b. *Ap. J.* 679:1433–42
Fujimoto MY, Taam RE. 1986. *Ap. J.* 305:246–50
Galloway DK, Muno MP, Hartman JM, Psaltis D, Chakrabarty D. 2008. *Ap. J. Suppl.* 179:360–422
Gandolfi S, Carlson J, Reddy S. 2012. *Phys. Rev. C* 85:032801

Gendreau KC, Arzoumanian Z, Okajima T. 2012. In *Space Telescopes and Instrumentation 2012: Ultraviolet to Gamma Ray*, ed. T Takahashi, SS Murray, J-WA den Herder. *Proc. SPIE Conf. Ser.* 8443:844313. Bellingham, WA: SPIE
Glendenning NK, ed. 2000. *Compact Stars: Nuclear Pysics, Particle Physics, and General Relativity*. New York: Springer-Verlag. 2nd ed.
Glendenning NK, Moszkowski SA. 1991. *Phys. Rev. Lett.* 67:2414–17
Glendenning NK, Schaffner-Bielich J. 1999. *Phys. Rev. C* 60:025803
Goriely S, Chamel N, Pearson JM. 2010. *Phys. Rev. C* 82:035804
Grindlay JE, Camilo F, Heinke CO, et al. 2002. *Ap. J.* 581:470–84
Guillot S, Rutledge RE. 2014. *Ap. J. Lett.* 796:L3
Guillot S, Rutledge RE, Brown EF. 2011. *Ap. J.* 732:88
Guillot S, Servillat M, Webb NA, Rutledge RE. 2013. *Ap. J.* 772:7
Güver T, Özel F. 2013. *Ap. J. Lett.* 765:L1
Güver T, Özel F, Cabrera-Lavers A, Wroblewski P. 2010a. *Ap. J.* 712:964–73
Güver T, Özel F, Psaltis D. 2012a. *Ap. J.* 747:77
Güver T, Psaltis D, Özel F. 2012b. *Ap. J.* 747:76
Güver T, Wroblewski P, Camarota L, Özel F. 2010b. *Ap. J.* 719:1807–12
Haensel P, Zdunik JL, Schaefer R. 1986. *Astron. Astrophys.* 160:121–28
Harris WE. 1996. *Astron. J.* 112:1487
Harrison BK, Thorne KS, Wakano M, Wheeler JA. 1965. *Gravitation Theory and Gravitational Collapse*. Chicago: Chicago Univ. Press. 1st ed.
Hebeler K, Lattimer JM, Pethick CJ, Schwenk A. 2010. *Phys. Rev. Lett.* 105:161102
Heger A, Cumming A, Galloway DK, Woosley SE. 2007. *Ap. J. Lett.* 671:L141–44
Heinke CO, Cohn HN, Lugger PM, et al. 2014. *MNRAS* 444:443–56
Heinke CO, Rybicki GB, Narayan R, Grindlay JE. 2006. *Ap. J.* 644:1090–103
Hessels JWT, Possenti A, Bailes M, et al. 2014. *Proc. Adv. Astrophys. Sq. Kilometre Array, Giardini Naxos, Italy, June 8–13*, PoS(AASKA14)047. **http://pos.sissa.it/archive/conferences/215/047/AASKA14_047.pdf**
Hessels JWT, Ransom SM, Stairs IH, et al. 2006. *Science* 311:1901–4
Hewish A, Bell SJ, Pilkington JDH, Scott PF, Collins RA. 1968. *Nature* 217:709–13
Hotokezaka K, Kyutoku K, Okawa H, Shibata M, Kiuchi K. 2011. *Phys. Rev. D* 83:124008
Hulse RA, Taylor JH. 1975. *Ap. J. Lett.* 195:L51–53
Itoh N. 1970. *Prog. Theoret. Phys.* 44:291
Jacoby BA, Bailes M, van Kerkwijk MH, et al. 2003. *Ap. J. Lett.* 599:L99–102
Jacoby BA, Cameron PB, Jenet FA, et al. 2006. *Ap. J. Lett.* 644:L113–16
Jacoby BA, Hotan A, Bailes M, Ord S, Kulkarni SR. 2005. *Ap. J. Lett.* 629:L113–16
Janka HT, Langanke K, Marek A, Martínez-Pinedo G, Müller B. 2007. *Phys. Rep.* 442:38–74
Janssen GH, Stappers BW, Kramer M, et al. 2008. *Astron. Astrophys.* 490:753–61
Kajava JJE, Nättilä J, Latvala OM, et al. 2014. *MNRAS* 445:4218–34
Kaplan DB, Nelson AE. 1986. *Phys. Lett. B* 175:57–63
Kaplan DL, Boyles J, Dunlap BH, et al. 2014a. *Ap. J.* 789:119
Kaplan DL, van Kerkwijk MH, Koester D, et al. 2014b. *Ap. J. Lett.* 783:L23
Kasian LE. 2012. *Radio observations of two binary pulsars*. PhD thesis, Univ. Br. Columbia
Keith MJ, Jameson A, van Straten W, et al. 2010. *MNRAS* 409:619–27
Keith MJ, Johnston S, Ray PS, et al. 2011. *MNRAS* 414:1292–300
Kerr M, Camilo F, Johnson TJ, et al. 2012. *Ap. J. Lett.* 748:L2
Kiziltan B, Kottas A, De Yoreo M, Thorsett SE. 2013. *Ap. J.* 778:66
Klüpfel P, Reinhard PG, Bürvenich TJ, Maruhn JA. 2009. *Phys. Rev. C* 79:034310
Knispel B, Lyne AG, Stappers BW, et al. 2015. *Ap. J.* 806:140
Kojo T, Powell PD, Song Y, Baym G. 2015. *Phys. Rev. D* 91:045003
Kortelainen M, Lesinski T, Moré J, et al. 2010. *Phys. Rev. C* 82:024313
Kramer M, Stairs IH, Manchester RN, et al. 2006. *Science* 314:97–102
Kramer M, Stappers B. 2014. *Proc. Adv. Astrophys. Sq. Kilometre Array, Giardini Naxos, Italy, June 8–13*, PoS(AASKA14)036. **http://pos.sissa.it/archive/conferences/215/036/AASKA14_036.pdf**

Kramer M, Wex N. 2009. *Class. Quantum Gravity* 26:073001
Kumar P, Zhang B. 2015. *Phys. Rep.* 561:1–109
Kurkela A, Fraga ES, Schaffner-Bielich J, Vuorinen A. 2014. *Ap. J.* 789:127
Kuulkers E, den Hartog PR, in't Zand JJM, et al. 2003. *Astron. Astrophys.* 399:663–80
Lackey BD, Kyutoku K, Shibata M, Brady PR, Friedman JL. 2012. *Phys. Rev. D* 85:044061
Lamb FK, Boutloukos S, Van Wassenhove S, et al. 2009. *Ap. J. Lett.* 705:L36–39
Lattimer JM. 2012. *Annu. Rev. Nucl. Part. Sci.* 62:485–515
Lattimer JM, Prakash M. 2001. *Ap. J.* 550:426–42
Lattimer JM, Schutz BF. 2005. *Ap. J.* 629:979–84
Lattimer JM, Steiner AW. 2014. *Ap. J.* 784:123
Lazarus P. 2013. In *The PALFA Survey: Going to Great Depths to Find Radio Pulsars*, *IAU Symp. 291*, ed. J van Leeuwen, 8:35–40. Cambridge, UK: Cambridge Univ. Press
Leahy DA, Morsink SM, Cadeau C. 2008. *Ap. J.* 672:1119–26
Leahy DA, Morsink SM, Chou Y. 2011. *Ap. J.* 742:17
Leahy DA, Morsink SM, Chung YY, Chou Y. 2009. *Ap. J.* 691:1235–42
Lewin WHG, van Paradijs J, Taam RE. 1993. *Space Sci. Rev.* 62:223–389
Lindblom L. 1992. *Ap. J.* 398:569–73
Link B, Epstein RI, Lattimer JM. 1999. *Phys. Rev. Lett.* 83:3362–65
Lo KH, Miller MC, Bhattacharyya S, Lamb FK. 2013. *Ap. J.* 776:19
London RA, Taam RE, Howard WM. 1986. *Ap. J.* 306:170–82
Lorimer DR. 2008. *Living Rev. Relativ.* 11:8
Lynch RS, Boyles J, Ransom SM, et al. 2013. *Ap. J.* 763:81
Lynch RS, Freire PCC, Ransom SM, Jacoby BA. 2012. *Ap. J.* 745:109
Lyne AG, Burgay M, Kramer M, et al. 2004. *Science* 303:1153–57
Madej J, Joss PC, Różańska A. 2004. *Ap. J.* 602:904–12
Majczyna A, Madej J. 2005. *Acta Astron.* 55:349–66
Majczyna A, Madej J, Joss PC, Różańska A. 2005. *Astron. Astrophys.* 430:643–54
Manchester RN, Hobbs GB, Teoh A, Hobbs M. 2005. *Astron. J.* 129:1993–2006
Manchester RN, Lyne AG, Camilo F, et al. 2001. *MNRAS* 328:17–35
Martinez JG, Stovall K, Freire PCC, et al. 2015. *Ap. J.* 812:143
Metzger BD, Martínez-Pinedo G, Darbha S, et al. 2010. *MNRAS* 406:2650–62
Miller MC, Lamb FK. 1998. *Ap. J. Lett.* 499:L37–40
Miller MC, Lamb FK, Psaltis D. 1998. *Ap. J.* 508:791–830
Morales J, Pandharipande VR, Ravenhall DG. 2002. *Phys. Rev. C* 66:054308
Morrison IA, Baumgarte TW, Shapiro SL, Pandharipande VR. 2004. *Ap. J. Lett.* 617:L135–38
Morsink SM, Leahy DA. 2011. *Ap. J.* 726:56
Morsink SM, Leahy DA, Cadeau C, Braga J. 2007. *Ap. J.* 663:1244–51
Mukherjee A. 2009. *Phys. Rev. C* 79:045811
Müller H, Serot BD. 1996. *Nucl. Phys. A* 606:508–37
Muno MP, Özel F, Chakrabarty D. 2002. *Ap. J.* 581:550–61
Muno MP, Özel F, Chakrabarty D. 2003. *Ap. J.* 595:1066–76
Müther H, Prakash M, Ainsworth TL. 1987. *Phys. Lett. B* 199:469–74
Nakar E. 2007. *Phys. Rep.* 442:166–236
Nath NR, Strohmayer TE, Swank JH. 2002. *Ap. J.* 564:353–60
Nättilä J, Steiner AW, Kajava JJE, Suleimanov VF, Poutanen J. 2016. *Astron. Astrophys.* 591:A25
Oppenheimer JR, Volkoff GM. 1939. *Phys. Rev.* 55:374–81
Orosz JA, Kuulkers E. 1999. *MNRAS* 305:132–42
Özel F. 2001. *Ap. J.* 563:276–88
Özel F. 2006. *Nature* 441:1115–17
Özel F. 2013. *Rep. Prog. Phys.* 76:016901
Özel F, Baym G, Güver T. 2010a. *Phys. Rev. D* 82:101301
Özel F, Gould A, Güver T. 2012a. *Ap. J.* 748:5
Özel F, Psaltis D. 2009. *Phys. Rev. D* 80:103003

Özel F, Psaltis D. 2015. *Ap. J.* 810:135
Özel F, Psaltis D, Güver T. 2015. *Ap. J.* Submitted. arXiv:1509.02924
Özel F, Psaltis D, Güver T, et al. 2016. *Ap. J.* 820:28
Özel F, Psaltis D, Narayan R, Santos Villarreal A. 2012b. *Ap. J.* 757:55
Özel F, Psaltis D, Ransom S, Demorest P, Alford M. 2010b. *Ap. J. Lett.* 724:L199–202
Paczynski B. 1983. *Ap. J.* 267:315–21
Page D. 1995. *Ap. J.* 442:273–85
Page D, Reddy S. 2006. *Annu. Rev. Nucl. Part. Sci.* 56:327–74
Pandharipande VR, Pethick CJ, Thorsson V. 1995. *Phys. Rev. Lett.* 75:4567–70
Pechenick KR, Ftaclas C, Cohen JM. 1983. *Ap. J.* 274:846–57
Piekarewicz J, Agrawal BK, Colò G, et al. 2012. *Phys. Rev. C* 85:041302
Portegies Zwart S, van den Heuvel EPJ, van Leeuwen J, Nelemans G. 2011. *Ap. J.* 734:55
Potekhin AY, Fantina AF, Chamel N, Pearson JM, Goriely S. 2013. *Astron. Astrophys.* 560:A48
Poutanen J, Beloborodov AM. 2006. *MNRAS* 373:836–44
Poutanen J, Gierliński M. 2003. *MNRAS* 343:1301–11
Poutanen J, Nättilä J, Kajava JJE, et al. 2014. *MNRAS* 442:3777–90
Prince TA, Anderson SB, Kulkarni SR, Wolszczan A. 1991. *Ap. J. Lett.* 374:L41–44
Psaltis D, Chakrabarty D. 1999. *Ap. J.* 521:332–40
Psaltis D, Özel F. 2014. *Ap. J.* 792:87
Psaltis D, Özel F, Chakrabarty D. 2014. *Ap. J.* 787:136
Psaltis D, Özel F, DeDeo S. 2000. *Ap. J.* 544:390–96
Raithel CA, Özel F, Psaltis D. 2016. *Phys. Rev. C* 93:032801
Ransom SM, Hessels JWT, Stairs IH, et al. 2005. *Science* 307:892–96
Ransom SM, Ray PS, Camilo F, et al. 2011. *Ap. J. Lett.* 727:L16
Ransom SM, Stairs IH, Archibald AM, et al. 2014. *Nature* 505:520–24
Rawls ML, Orosz JA, McClintock JE, et al. 2011. *Ap. J.* 730:25
Read JS, Baiotti L, Creighton JDE, et al. 2013. *Phys. Rev. D* 88:044042
Read JS, Markakis C, Shibata M, et al. 2009. *Phys. Rev. D* 79:124033
Reardon DJ, Hobbs G, Coles W, et al. 2016. *MNRAS* 455:1751–69
Rikovska Stone J, Guichon PAM, Matevosyan HH, Thomas AW. 2007. *Nucl. Phys. A* 792:341–69
Roberts MSE, McLaughlin MA, Gentile PA, et al. 2014. In *Proc. 2014 Fermi Symp. - eConf C14102.1*. arXiv:1502.07208
Roca-Maza X, Centelles M, Viñas X, Warda M. 2011. *Phys. Rev. Lett.* 106:252501
Rutledge RE, Bildsten L, Brown EF, Pavlov GG, Zavlin VE. 2001. *Ap. J.* 551:921–28
Ryba MF, Taylor JH. 1991. *Ap. J.* 371:739–48
Schulze HJ, Lejeune A, Cugnon J, Baldo M, Lombardo U. 1995. *Phys. Lett. B* 355:21–26
Splaver EM. 2004. *Long-term timing of millisecond pulsars*. PhD thesis, Princeton Univ.
Stairs IH. 2003. *Living Rev. Relativ.* 6:5
Steiner AW, Lattimer JM, Brown EF. 2010. *Ap. J.* 722:33–54
Steiner AW, Lattimer JM, Brown EF. 2013. *Ap. J. Lett.* 765:L5
Stergioulas N, Friedman JL. 1995. *Ap. J.* 444:306–11
Stovall K, Lynch RS, Ransom SM, et al. 2014. *Ap. J.* 791:67
Strohmayer TE, Zhang W, Swank JH. 1997. *Ap. J. Lett.* 487:L77–80
Strohmayer TE, Zhang W, Swank JH, et al. 1996. *Ap. J. Lett.* 469:L9
Suleimanov V, Poutanen J, Werner K. 2011. *Astron. Astrophys.* 527:A139
Suleimanov V, Poutanen J, Werner K. 2012. *Astron. Astrophys.* 545:A120
Swiggum JK, Rosen R, McLaughlin MA, et al. 2015. *Ap. J.* 805:156
Sztajno M, Fujimoto MY, van Paradijs J, et al. 1987. *MNRAS* 226:39–55
Tamii A, Poltoratska I, von Neumann-Cosel P, et al. 2011. *Phys. Rev. Lett.* 107:062502
Taylor JH, Fowler LA, McCulloch PM. 1979. *Nature* 277:437–40
Thorsett SE, Chakrabarty D. 1999. *Ap. J.* 512:288–99
Tolman RC. 1934. *Relativity, Thermodynamics, and Cosmology*. New York: Dover
Tolman RC. 1939. *Phys. Rev.* 55:364–73

Trippa L, Colò G, Vigezzi E. 2008. *Phys. Rev. C* 77:061304
Tsang MB, Zhang Y, Danielewicz P, et al. 2009. *Phys. Rev. Lett.* 102:122701
van Kerkwijk MH, Breton RP, Kulkarni SR. 2011. *Ap. J.* 728:95
van Kerkwijk MH, Kulkarni SR. 1999. *Ap. J. Lett.* 516:L25–28
van Leeuwen J, Kasian L, Stairs IH, et al. 2015. *Ap. J.* 798:118
van Paradijs J. 1979. *Ap. J.* 234:609–11
Verbiest JPW, Bailes M, van Straten W, et al. 2008. *Ap. J.* 679:675–80
Verbunt F, Freire PCC. 2014. *Astron. Astrophys.* 561:A11
Watts A, Andersson N, Chakrabarty D, et al. 2016. *Rev. Mod. Phys.* 88:021001
Watts AL. 2012. *Annu. Rev. Astron. Astrophys.* 50:609–40
Webb NA, Barret D. 2007. *Ap. J.* 671:727–33
Weinberg N, Miller MC, Lamb DQ. 2001. *Ap. J.* 546:1098–106
Weisberg JM, Nice DJ, Taylor JH. 2010. *Ap. J.* 722:1030–34
Wex N. 2014. In *Frontiers in Relativistic Celestial Mechanics*, Vol. 2, *Applications and Experiments*, ed. S Kopeikein, pp. 61–124. Berlin: de Gruyter
Wheeler JA. 1966. *Annu. Rev. Astron. Astrophys.* 4:393–402
Witten E. 1984. *Phys. Rev. D* 30:272–85
Yagi K, Stein LC, Pappas G, Yunes N, Apostolatos TA. 2014. *Phys. Rev. D* 90:063010
Yagi K, Yunes N. 2013. *Phys. Rev. D* 88:023009
Zamfir M, Cumming A, Galloway DK. 2012. *Ap. J.* 749:69
Zavlin VE. 2006. *Ap. J.* 638:951–62
Zavlin VE. 2007. *Ap. Space Sci.* 308:297–307
Zavlin VE, Pavlov GG, Shibanov YA. 1996. *Astron. Astrophys.* 315:141–52
Zhu WW, Stairs IH, Demorest PB, et al. 2015. *Ap. J.* 809:41

Annual Review of Astronomy and Astrophysics

Volume 54, 2016

Contents

A Fortunate Half-Century
Jeremiah P. Ostriker 1

The Remnant of Supernova 1987A
Richard McCray and Claes Fransson 19

Astrophysics with Extraterrestrial Materials
Larry R. Nittler and Fred Ciesla 53

Red Clump Stars
Léo Girardi 95

Accretion onto Pre-Main-Sequence Stars
Lee Hartmann, Gregory Herczeg, and Nuria Calvet 135

Interstellar Hydrides
Maryvonne Gerin, David A. Neufeld, and Javier R. Goicoechea 181

The Quest for B Modes from Inflationary Gravitational Waves
Marc Kamionkowski and Ely D. Kovetz 227

Gravitational Instabilities in Circumstellar Disks
Kaitlin Kratter and Giuseppe Lodato 271

The Evolution of the Intergalactic Medium
Matthew McQuinn 313

The Magellanic Stream: Circumnavigating the Galaxy
Elena D'Onghia and Andrew J. Fox 363

Masses, Radii, and the Equation of State of Neutron Stars
Feryal Özel and Paulo Freire 401

The Eccentric Kozai-Lidov Effect and Its Applications
Smadar Naoz 441

Protostellar Outflows
John Bally 491

The Galaxy in Context: Structural, Kinematic, and Integrated Properties
Joss Bland-Hawthorn and Ortwin Gerhard 529

Structure and Kinematics of Early-Type Galaxies from Integral Field Spectroscopy
Michele Cappellari 597

Six Decades of Spiral Density Wave Theory
Frank H. Shu 667

Gamma-Ray Observations of Active Galactic Nuclei
Grzegorz (Greg) Madejski and Marek Sikora 725

Galaxies in the First Billion Years After the Big Bang
Daniel P. Stark 761

Indexes

Cumulative Index of Contributing Authors, Volumes 43–54 805

Cumulative Index of Article Titles, Volumes 43–54 808

Errata

An online log of corrections to *Annual Review of Astronomy and Astrophysics* articles may be found at http://www.annualreviews.org/errata/astro